RESAERCH ARTICLE

Analysis of the Current-Voltage Curves and Saturation Currents in Burner-Stabilized Premixed Flames with Detailed Ion Chemistry and Transport Models

Memdouh Belhi [a*], Jie Han[a], Tiernan A. Casey[b], Jyh-Yuan Chen[b], Hong G. Im [a], S. Mani Sarathy[a] and Fabrizio Bisetti[c]

[a] *King Abdullah University of Science and Technology, Clean Combustion Research Center, Thuwal 23955, Saudi Arabia*

[b] *Department of Mechanical Engineering, University of California, Berkeley, CA 94720-1740, USA*

[c] *Department of Aerospace Engineering and Engineering Mechanics, University of Texas at Austin, Austin, TX 78712-1085, USA*

(*Compiled February 28, 2018*)

Current-voltage, or $i-V$, curves are used in combustion to characterize the ionic structure of flames. The objective of this paper is to develop a detailed modeling framework for the quantitative prediction of the $i-V$ curves in methane/air flames. Ion and electron transport coefficients were described using methods appropriate for charged species interactions. An ionic reaction mechanism involving cations, anions and free electrons was used, together with up-to-date rate coefficients and thermodynamic data. Because of the important role of neutral CH species in the ion production process, its prediction by the detailed AramcoMech 1.4 mechanism was optimized by using available experimental measurements. Model predictions were evaluated by comparing to i-V curves measured in atmospheric-pressure, premixed, burner-stabilized flames. A detailed evaluation of the reliability of ion kinetic and transport parameters adopted was performed. The model provides good quantitative agreement with experimental data for various conditions.

Keywords: 1D premixed flames; $i-V$ curve; saturation; charged species, CH predictions

1. Introduction

Studying electric currents in flames has many practical applications in combustion. For instance, the presence of ions in flames allows early detection of important combustion characteristics such as ignition [1], flame position [2] and the mixture equivalence ratio [3,4]. Ions in flames may also be exploited for combustion stabilization [5,6] and the reduction of pollutant emissions [7] via the application of external electric fields. Consequently, there is strong interest in computational models for predicting the currents of charged species in flames [4,8,9]. We developed and evaluated such a model in this work.

In hydrocarbon flames, positive ions and electrons are produced naturally by a chemi-ionization process [10]. The peak ion number density is correlated with the maximum heat release rate [11], and varies between 10^{16} and 10^{17} m^{-3} for atmospheric flames depending on the fuel and equivalence ratio [12]. Total positive and negative

*Corresponding author. Email: memdouh.belhi@kaust.edu.sa

charges decrease along a flame's burned gas, as a result of positive ions recombining with free electrons [10,13,14]. Negative ions, primarily OH^- and $O_2{}^-$, are present in the reaction zone of hydrocarbon flames in air, and they are generally attributed to associative and dissociative electron attachment reactions, such as $O_2 + e^- + M \rightleftharpoons O_2{}^- + M$ and $H_2O + e^- \rightleftharpoons OH^- + H$, respectively [15–17].

Development of reliable ionization mechanisms is limited by the scarcity of quantitative measurements of charged species [16]. The accuracy of simulations also relies strongly on the kinetic and transport properties of the charged species. In particular, the chemi-ionization and recombination rate constants are paramount to the quantitative prediction of the total positive and negative charges in a flame [9,13,14,18]. However, the current literature offers widely different values for these rates, showing important contrasts in the presumed temperature dependence [19]. The kinetic data to determine the contribution of anions to the total negative charge are even more uncertain. Furthermore, neutral radicals CH and O play a crucial role in producing the charged species [13,18,20] and they should be predicted accurately to simulate the concentrations of charge carriers in flames. Unfortunately, many existing kinetic mechanisms show large differences in CH concentrations [21–23].

In view of these limitations, current-voltage (i-V) curves of flames seem to be a valuable tool to evaluate and optimize ionization models [3,4,24–27]. The i-V curve describes the evolution of the electric current drawn from the flame with the bias voltage applied across the reaction zone. The current increases monotonically with the applied voltage up to a threshold saturation condition, which is related to the depletion of electrons and ions from the flame [3,27]. The applied electric potential required to reach the saturation and the corresponding electric current are defined as the saturation voltage ΔV_s and the saturation current i_s, respectively.

Based on numerical simulations using simplified chemistry and transport models, Han et al. [27] have developed an analytical model to describe the $i-V$ characteristics of one-dimensional premixed flames. The analytical model shows that the saturation voltage depends both on the flame's proximity to the electrodes, and on the transport coefficients of charged species. It was also confirmed that the saturation current can be accurately computed by the integration of the ion production rate between the electrodes. The proposed formulas are useful to determining the ruling factors in optimizing ionization mechanisms against experiments.

Speelman et al. [4] investigated the $i-V$ curves experimentally and numerically in atmospheric-pressure burner-stabilized methane/air flames with the aim of proposing optimized ion chemistry and transport models. Based on a sensitivity analysis, Speelman et al. [4] proposed optimized values for the ion chemi-ionization and recombination rate constants and diffusivities of electrons and H_3O^+ cation. While the optimized model provides a very good agreement with comparison to experiment data [28], the fitted values do not account for potential error in the predictions of CH, which may contribute to their uncertainty.

The present work proposes up-to-date detailed chemistry and transport models for the quantitative prediction of i-V curves in methane/air burner-stabilized flames, and includes substantial comparisons against two available experimental data sets [3,4]. Furthermore, recognizing the important role of CH in the formation of ions and electrons, the present work features a detailed optimization of the CH chemistry against three sets of CH measurements in premixed flames [21–23]. A detailed evaluation of key ion chemistry and transport parameters is presented. The approach adopted in this work is different to that of Speelamn et al. [4] in the sense that all rate constants and transport coefficients employed were validated independently from a variety of

literature sources.

This paper begins with a description of the flame parameters and computational setup considered. Numerical methodology and chemistry mechanism are presented next. Following is an evaluation of the model's predictions with comparison to the measurements by Speelman et al. [3,4]. The sensitivity of the saturation features to CH predictions, chemi-ionization and recombination rates, and transport coefficients of charged species is respectively investigated. The optimization process of CH is presented in Appendix B.

2. Configuration

Laminar burner-stabilized flames are very often used to study chemical kinetics in combustion because they are effectively one-dimensional and can be made very steady [29], thus facilitating simulations with detailed models. As a baseline for this study, we used two laminar flat premixed burner-stabilized flames that were previously investigated by Speelman et al. [3,4]. These flames were considered since detailed measurements of $i-V$ curves and saturation currents were provided for various equivalence ratios and electrode separation distances. The flames were also simulated by Speelman et al. [3,4]. The results in this work can thus be compared with both experimental and numerical data.

The flames burned premixed mixtures of methane-air at atmospheric conditions. A DC potential was applied to a wire mesh electrode placed downstream and parallel to the burner surface, which acted as the ground electrode. The current was measured across a precision resistor assuming that all charges drifted downstream are consumed at the surface of the high-tension electrode. This is justified by the fact that the movement of charged species is controlled mainly by the drift flux vectors oriented toward to the electrode matrix. A small amount of charged species may pass through the mesh due to the convection or the Fickian diffusion, but this does not affect significantly the measured current. The radial extent of the electrodes is sufficiently large compared to the separation so that edge effects and associated drift fluxes (current) of charged species in the radial direction are insignificant. The problem can thus be approximated as one-dimensional and steady [3,4,30,31].

In the first set of experiments, Speelman et al. [3] used a McKenna burner with a diameter of $D = 6$ cm (Holthuis & Associates [32]). The feed gases had a temperature of 288 K and the equivalence ratio was varied between 0.7 and 1.35. The reactant mass flow rate for each equivalence ratio is provided in Ref. [28]. The potential was varied from -0.35 to 0.35 kV, and the $i-V$ measurements were repeated for three electrode separation distances: 0.37, 1 and 2 cm.

The second set of experiments [4] dealt with flames stabilized on a heat flux burner [33] with a diameter of D =3 cm. The reactant mass flow rate was adjusted so the inflow velocity was equal to the laminar burning velocity of a methane/air flame burning at 298 K and 1 atm, while the temperature of the feed gases was 350 K. The flame stoichiometry was varied between 0.7 and 1.2 and the potential was varied from -0.25 to 0.25 kV. The charged electrode was placed 1 cm above the burner surface. For the sake of clarity, the terms *McK flame* and *HFB flame* will be used to distinguish the results of the first [3] and second [4] set of experiments.

The flames were simulated as one-dimensional steady burner-stabilized flames using the PREMIX code [29] with a known mass flow rate: $\dot{m} = \rho u$, where u and ρ are the mass-averaged bulk velocity and density, respectively. The gas density was calculated

by the classic perfect gas law assuming a constant pressure ($p = 1$ atm). The temperature, T, was determined by the energy conservation equation. Positive or negative DC potential (ΔV) was imposed at the downstream boundary ($x = L$), while the burner boundary ($x = 0$) was maintained at zero voltage. The polarity was considered to be positive if $\Delta V > 0$ and negative if $\Delta V < 0$. Fig. 1 illustrates a schematic of the numerical configuration.

3. Numerical methodology

Several modifications were implemented in PREMIX [29] to allow for the simulation of electric currents in one-dimensional burner stabilized flames. First, the electric potential was added to the boundary value solver as an additional variable and its distribution was determined by the Poisson equation as:

$$\frac{d^2V}{dx^2} = -\frac{e}{\epsilon_0}\sum_{k}^{M} q_k n_k, \tag{1}$$

where V is the electric potential, x is the space coordinate, $e = 1.602 \times 10^{19}$ C is the elementary charge, $\epsilon_0 = 8.314 \times 10^{12}$ F/m is the vacuum permittivity, M is the number of species considered in the reaction mechanism, n_k and q_k are the number density and the charge number of species k, respectively.

Second, the mass flux in the transport equations for charged species was modified to include the drift diffusion flux ($W_d = {}^{q_k}/_{|q_k|}\mu_k E \rho Y_k$) due to the electric field:

$$\dot{m}\frac{dY_k}{dx} + \frac{d}{dx}\left(-D_k\frac{\rho Y_k}{X_k}\frac{dX_k}{dx} + \frac{q_k}{|q_k|}\mu_k E \rho Y_k\right) = W_k\dot{\omega}_k, \tag{2}$$

where Y_k, X_k, W_K and $\dot{\omega}_k$ are the mass fraction, the molar fraction, the molar mass and the molar source term of species k, respectively. The electric field strength E was determined from the gradient of the voltage as:

$$E = -\frac{dV}{dx}. \tag{3}$$

Ion mobilities (μ_k) and diffusivities (D_k) were determined using mixture-average rules as [34,35]:

$$\frac{1}{\mu_k} = \sum_{j}^{M}\frac{X_j}{\mu_{kj}}, \tag{4}$$

$$D_k = \frac{\sum_{j\neq k}^{M} X_j W_j}{\overline{W}\sum_{j\neq k}^{M} X_j/D_{kj}}, \tag{5}$$

where $\overline{W}$ is the mixture molar mass. The binary mobility and diffusivity were obtained

by [34,36]:

$$\mu_{kj} = \frac{3}{16}\frac{|q_k|e}{\sigma_{kj}N}\sqrt{\frac{2\pi N_A}{k_b T m_{kj}}}, \tag{6}$$

$$D_{kj} = \frac{3}{16}\frac{1}{\sigma_{kj}N}\sqrt{\frac{2\pi N_A k_b T}{m_{kj}}}, \tag{7}$$

where $m_{kj} = m_k m_j/(m_k + m_j)$ is the reduced molar mass, $N_A = 6.022{\times}10^{\ 23}$ mol^{-1} is the Avogadro number, N is the number density of the background gas mixture and $k_b = 1.381 \times 10^{-23}$ J·K^{-1} is the Boltzmann constant.

The (n,6,4) [34] and Coulomb [37] interaction potentials describing ion-neutral and ion-charge interactions, respectively, were used to compute the binary collision cross sections (σ_{kj}). The detailed description of the calculation method of the collision cross sections and required parameters is presented in Ref. [38], where the accuracy of the model predictions is evaluated against experimental data for the mobility of selected ions in pure gases.

Analysis of non-thermal electron transport properties in methane-air flames suggests a breakdown threshold of 140 Td [39]. Since the reduced electric field strength does not exceed this threshold in the configurations considered in our work, electrons are assumed to be thermal. The electron mobility was computed as a function of temperature and mixture composition by [40]:

$$\mu_e = \frac{2}{3}\frac{e}{p\sum_{j=1}^{M} X_j \sigma_j}\sqrt{\frac{2ek_bT}{\pi m}}, \tag{8}$$

where m $= 9.109 \times 10^{-31}$ kg is the mass of the electron. The effective cross-sections of electron-neutral pairs (σ_j) were collected from the LXcat repository [41]. The electron diffusivity was estimated from the electron mobility using Einstein's relation:

$$\frac{D_e}{\mu_e} = \frac{k_B T}{e}. \tag{9}$$

Sensitivity of the electric currents to the transport properties of ions and electrons is discussed in Section 5.2.2.

Boundary conditions proposed in Ref. [42] were adopted for the transport equations of charged species. It was assumed that the mass fractions of negative charges are zero at the cathode and their gradients are zero at the anode. On the contrary, the mass fractions of cations were assumed to be zero at the anode and their gradients are zero at the cathode. These assumptions are based on the drift of the charged species at the electrodes and are equivalent to the boundary conditions used in the plasma community for one-dimensional discharges as proposed in Ref. [43]. The boundary conditions corresponding to our configuration are listed in Tab. 1.

An external electric field can affect the flame dynamics through an electric force, which appears in the momentum equation. The impact of the electric force on the

pressure field was computed by using the momentum equation as:

$$\frac{\partial p}{\partial x} = -\dot{m}\frac{\partial u}{\partial x} + F_e, \tag{10}$$

where viscous terms are neglected [44]. Since a one-dimensional approach was considered, the momentum equation is uncoupled from the other equations and serves only to determine the pressure field. The electric force acting on the flow dynamics is given by Coulomb's law as:

$$F_e = eE\sum_{k}^{N} q_k n_k. \tag{11}$$

For all the simulations performed in this study, the electric force impacts the pressure difference across the flame, which is estimated to be of the order of 1 Pa [44], by less than 0.2 Pa. The pressure jump across the flame, with or without the electric field, is negligible compared to the background atmospheric pressure and does not have an appreciable effect on the density.

Small variations of around 0.1 mm in the stand-off distance of a flat burner-stabilized flame may be encountered in the presence of a DC electric field [45], but these do not significantly affect the i-V curves. Similar conclusions were demonstrated by the asymptotic analysis proposed by Paytal et al. [46], where the electric force effect in the droplet problem was found to act only to modify the radial pressure gradient with no implication on the flame. It should be noted, however, that the effects brought by the electric force are specific to the configuration and in more general circumstances the electric force could have an effect on the flame position. For instance, unlike the burner-stabilized flames considered here, counterflow systems may provide a low velocity environment near the reaction zone that allows for observing a sizable motion of the flame in the presence of electric forces [47–49].

The electric force can also affect the combustion through the ohmic heating, which acts as a heat source in the energy equation. The ohmic heating is defined as:

$$\Omega = eE\sum_{k}^{M} q_k n_k \left(u - \frac{D_k}{X_k}\frac{dX_k}{dx} + \frac{q_k}{|q_k|}\mu_k E\right). \tag{12}$$

It represents the work done on the charged particles due mainly to the electric drift flux. With increasing the voltage, the ohmic heating may cause a slight increase in the flame temperature as shown by Paytal et al. [46]. However, the effect of ohmic heating is negligible in flames subjected to sub-breakdown electric fields [42,50] and it was thus neglected in the present study.

A detailed analysis of the spatial distribution of charges, electric field, and potential in one-dimensional premixed flames using simplified transport and chemistry models was proposed in our previous study [27]. Simulations showed particularly the existence of an ion sheath at the cathode, in which the electric potential falls considerably. Also, at the anode, we observed a drop in the potential, which is smaller than that at the cathode. These sheaths were, of course, observed in the present work also.

The electric current characterizes the rate at which charges flow through the flame surface for a given bias voltage. It was computed by summing up the current density drawn from the flame (J) over the flame surface assumed to be equal to the burner

surface area:

$$i = \frac{\pi}{4} d^2 J. \tag{13}$$

The electric current density consists of the contributions from the convective, diffusive and drift fluxes summed over all the charged species:

$$J = e \sum_{k}^{M} q_k n_k \left(u - \frac{D_k}{X_k} \frac{dX_k}{dx} + \frac{q_k}{|q_k|} \mu_k E \right), \tag{14}$$

As a result of charge conservation, the current density is spatially uniform :

$$\frac{\partial J}{\partial x} = e N_A \sum_{k}^{M} q_k \dot{\omega_k} = 0, \tag{15}$$

This means that the current density is a flame property that depends only on the inflow, mixture properties and bias voltage. The i-V curve of a burner-stabilized flame is then a representation of the complex interaction of ion chemistry and transport in the presence of an electric field [4,27].

4. Chemistry mechanism

To describe the formation and consumption of charged species, the mechanism assembled by Prager et al. [8] was used, with updates to the ion reaction rates and charged species thermodynamic data according to the UMIST [19] and Burcat [51] databases, respectively. The updated ion chemistry mechanism is provided in Appendix A.

The mechanism accounts for 68 ion reactions including four cations (H_3O^+, $C_2H_3O^+$, CH_5O^+, HCO^+), six anions (O_2^-, O^-, OH^-, CHO_2^-, CHO_3^-, CO_3^-), and electrons. The ion chemistry pathways rely largely on the experimental measurements of ion profiles in a lean ($\Phi = 0.216$) methane/oxygen Bunsen-type flame by Goodings et al. [15,52]. The model reasonably predicted the qualitative distribution of positive ions in the lean flame investigated by Goodings et al. [15,52], but showed important shortcomings for negative ions. Comparisons to experimental data were only qualitative because the absolute ion concentrations were not provided in Refs. [15,52].

In the ion reaction mechanism, positive ions and electrons are produced as a result of:

$$CH + O \rightleftharpoons HCO^+ + e^-. \tag{R1}$$

The fast cation HCO^+ is immediately transformed into the hydronium ion H_3O^+ via a proton transfer reaction:

$$HCO^+ + H_2O \rightleftharpoons H_3O^+ + CO. \tag{R2}$$

The H_3O^+ cation recombines with electrons via four reactions to produce neutrals:

$$H_3O^+ + e^- \rightleftharpoons H_2O + H; \tag{R3a}$$

$$H_3O^+ + e^- \rightleftharpoons OH + H + H; \quad \text{(R3b)}$$

$$H_3O^+ + e^- \rightleftharpoons H_2 + OH; \quad \text{(R3c)}$$

$$H_3O^+ + e^- \rightleftharpoons O + H_2 + H. \quad \text{(R3d)}$$

The reactions presented above (R1, R2 and R3) were initially proposed in Refs. [10, 13,14], where they were found to be the main source of ions in hydrocarbon flames.

As a result of ion/molecule reactions, the H_3O^+ cation forms other positive ions ($C_2H_3O^+$, CH_5O^+) that were observed ahead of the reaction zone [52,53]. Because of the conservation of mass and charge, the transport of these cations can be omitted if the transport coefficients of all ions are assumed to be equivalent [9]. However, the ion mobility is inversely proportional to the molar mass of the species [38]. Therefore, the ions $C_2H_3O^+$ and CH_5O^+ have lower mobilities compared to that of H_3O^+ [38], and neglecting them may degrade the prediction of the total local positive charge and associated electric currents.

Electrons attach to selected neutral species (O_2, O, and OH) via three body reactions to generate anions ($O_2{}^-$, OH^-, and O^-):

$$A + B + e^- \rightleftharpoons A^- + B. \quad \text{(R4)}$$

Other anions ($CHO_2{}^-$, $CHO_3{}^-$, $CO_3{}^-$) are formed via ion/molecule reactions. Anions also participate in associative electron detachment reactions, such as: $O^- + O \rightleftharpoons O_2 + e^-$, which are an important route of anion loss in the burnt gases. Determination of concentration shares of electrons and negative ions is challenging due to the lack of experimental measurements and the uncertainty in the kinetic data. While it is commonly considered that electrons are the main carrier of the negative charge in flames [12,54–56], the accurate description of the negative ions with distinct chemical and transport characteristics is critical for describing the flame-electric field interaction under certain conditions [9,57].

As the formation of ions and electrons in hydrocarbon flames occurs via the interaction of CH and O radicals (R1), reliable predictions of $i-V$ curves can only be achieved if the CH and O distribution are predicted accurately. The analysis in Ref. [18] demonstrated that the mean and variance of the densities of both positive and negative charges are controlled by the rates of chemi-ionization as well as the rates of key neutral reactions involving the CH radical. However, significant discrepancies in the CH concentrations predicted by available chemistry kinetic mechanisms were observed in the literature [21–23].

The AramcoMech 1.4 chemical kinetic model [58,59], which contains 311 species and 1831 reactions, was designed to simulate the combustion chemistry of a comprehensive set of C1-C4 fuels over a wide range of pressures, temperatures and stoichiometries. It includes a large number of intermediates involved in the chemistry of the most abundant positive and negative ions detected in flames. Nevertheless, the ability of this mechanism to predict CH concentrations accurately has not been previously assessed.

Based on comparisons to experimental measurements [21], the values of two reaction rate constants in the AramcoMech 1.4 mechanism were modified using kinetic data from the literature, in order to improve the CH predictions. The AramcoMech 1.4 mechanism optimized to improve the CH predictions will be referred to as the Modified

AramcoMech 1.4 mechanism and used in the simulation of the $i-V$ curves. Detailed description of the modifications to the AramcoMech 1.4 mechanism and comparisons with experimental data are presented in Appendix B.

5. Analysis of $i-V$ curves in one-dimensional premixed flames

Figures 2 and 3 compare simulated i-V curves to experimental data and numerical results of Speelman et al. [3,4]. The $i-V$ curves obtained in the *HFB flame* with three equivalence ratios are shown in Fig. 2, while those obtained in the *Mck flame* with three inter-electrode distances at $\Phi = 1$ are shown in Fig. 3.

In the simulations of Speelman et al. [3,4], the GRIMech 3.0 mechanism [60] was combined with a simplified 3-step ion mechanism from Ref. [42] to represent the chemistry, and the Stockmayer potential [61] was used to model the transport coefficients of ions and electrons. The rate constants from Refs. [62] and [63] were used by Speelman et al. [3,4] to compute the overall rates of chemi-ionization (R1) and recombination process (R3a, R3b, R3c and R3d), respectively, and they are different from the rate constants used in the simulations presented here. In order to improve the agreement between simulations and experimental data in the *HFB flame*, Speelman et al. [4] proposed fitted values for the chemi-ionization and recombination rate constants and the diffusivity coefficients of electrons and H_3O^+ cations. This optimized mechanism was also used by Speelman et al. to compute the *Mck flames* [28].

The models qualitatively reproduce the evolution of the electric current with the applied electric potential and capture the saturation phenomenon in both *HFB* and *Mck flames*. Our predictions of the $i-V$ curves are in good agreement with the experimental data for both configurations. The agreement of our results with experimental data is generally an improvement over that of the non-optimized model used by Speelman et al. [3,4] for all equivalence ratios and electrode distances considered. This may be due to a better prediction of CH concentrations by our model than that by the GRIMech 3.0 mechanism used by Speelman et al. [3,4]. Moreover, the transport coefficients of charged species in Refs. [3,4] were modeled using the Stockmayer potential [61], which is not suitable for ions and electrons [8,38]. This may help explain the steeper slopes of the i-V curves obtained with the transport coefficients adopted by Speelman et al. [4]. Finally, differences between the two models may also be caused by differences in the chemi-ionization and recombination rate constants adopted.

As shown in Fig. 2 and Fig. 3, the optimized mechanism provides the best agreement with experimental data. Based on the results presented in our work, we highlight that these optimized rate constants are likely to compensate the inaccuracies in the prediction of the CH radical by the GRIMech 3.0 mechanism, which was used by Speelman et al. [3,4]. The overestimation of CH by GRIMech 3.0 is documented in Appendix B. Furthermore, as shown in this work, there exist a tight coupling between the recombination rate constant and the mobility of electrons, so that one may find an optimal, albeit incorrect combination of the values of these two parameters which describes well positive saturation voltages. In this work, we adopted a different approach and employed rate constants and transport coefficients, which were validated independently from a variety of sources.

5.1. Saturation currents

By summing the species current densities (see Eqs. 14 and 15) over the positive ions, we obtain:

$$\frac{dJ^+}{dx} = eN_A\dot{\omega}^+, \tag{16}$$

where J^+ and $\dot{\omega}^+$ are the total current density and molar source term of positive ions, respectively. By neglecting the reverse rates of the recombination reactions (R3a-R3d) and integrating Eq. 16 over the space inter-electrode, we obtain:

$$J = \int_{x=0}^{x=L} \frac{dJ^+}{dx} dx = eN_A \int_{x=0}^{x=L} \left(k_c[\mathrm{CH}][\mathrm{O}] - k_r[\mathrm{H_3O^+}][\mathrm{e^-}]\right) dx, \tag{17}$$

where $[\cdot]$ denotes molar concentration and k_c and k_r are the chemi-ionization and recombination rate constants, respectively.

Saturation of the current occurs when the voltage applied across the flame is sufficiently high so that all ions and electrons generated through chemi-ionization (R1) are removed from the flame. As a result, the concentrations of ions and electrons decrease and the recombination of positive ions with electrons is negligible at saturation. The saturation current density is thus estimated by [4,27]:

$$J_s = eN_A \int_{x=0}^{x=L} k_c[\mathrm{CH}][\mathrm{O}]dx. \tag{18}$$

Eq. 17 is then written as:

$$J = J_s - eN_A \int_{x=0}^{x=L} k_r[\mathrm{H_3O^+}][\mathrm{e^-}]dx. \tag{19}$$

The last two equations show the importance of the chemi-ionization and recombination rate constants in the simulation of currents drawn from flames. Note that, since the CH radical is produced in a thin layer, much smaller than the separation distance, the saturation current is independent of the wire mesh position.

As shown by Eq. 18, the saturation current reflects the number of ions or electrons produced in the flame and its accurate prediction is therfore an important criterion by which to assess the quality of the models. The saturation currents for various equivalence ratios are compared to the measured data from the *HFB flame* and *McK flame* in Figs. 4(b) and 4(a), respectively. Generally, the models reproduce well the dependence of the saturation current on the equivalence ratio. The maximum saturation currents from models are obtained at an equivalence ratio of 1.1 in agreement with the experiments. Our model delivers improved prediction of the saturation currents over the non-optimized model used by Speelman et al. [3,4].

Our results show very good agreement with the measured data in the *HFB* flame. The relative differences between the experimental saturation currents from the *HFB flame* and predictions from our model fall between 2% and 20% over a wide range of equivalence ratios. The agreement of the predictions in the *McK flame* is less satisfactory with a relative difference that varies between 3% and 50% in comparison to the experimental data. The non-optimized chemistry model used by Speelman et al. [3,4] provides much higher saturation currents for all equivalence ratios, featuring mean

relative differences of more than 160% and 120% compared to the experimental values in the *McK flame* and the *HFB flame*, respectively.

The saturation currents obtained from the integration of the ion production rate over the space between electrodes are also shown in Figs. 4(b) and 4(a). They correspond to the saturation currents determined from the fluxes of charged species. This confirms that the magnitude of the saturation current drawn from the flame is determined solely by the rate of formation of the charged species.

Despite the fact that the two experiments [3,4] use similar pressure and temperature, the saturation current densities in the *McK flame* are lower by a factor that varies between 0.1 and 0.9 depending on the equivalence ratio. We are of the opinion that the differences are caused by differences in the reactant mass flow rates. Since the flames investigated here are stabilized on the burner, temperature and species profiles do not depend on the properties of the combustible mixture alone, but also on the interaction of the flame with the burner. The properties of the burner stabilized flames and concentrations of species at the burner surface are very sensitive to the reactant mass flow rate. With the exception of the leanest stoichiometry ($\Phi = 0.7$), the mass flow rates used in the *McK flame* are lower than those of the *HFB flame* by a factor that ranges between 0.3 and 0.8. As the mass flow rates in the *Mck flame* are relatively low, the flame is closer to the burner. As a result, the interaction of the flame with the burner is more significant, leading to a higher sensitivity of species concentrations and temperature to the inlet boundary conditions. Errors originating from the modeling of this interaction might account for the greater differences between experimental and numerical saturation currents.

Equation 18 shows that the saturation current is independent of the transport of charged particles and is solely a function of the chemi-ionization rate and predictions of CH and O. The sensitivity of the saturation current to the CH predictions and the value of the chemi-ionization rate constant is discussed, respectively, in the next two sections.

5.1.1. On the role of CH

To study the effect of CH predictions on the $i-V$ curves, the *McK flame* at $\Phi = 1$ was modeled using three mechanisms: the GRIMech 3.0 mechanism, the AramcoMech 1.4 mechanism and the Modified AramcoMech 1.4 mechanism. All ion chemistry and transport model parameters were kept the same.

Figure 5 compares the $i-V$ curves and profiles of CH mole fractions obtained with the three reaction models. Significant differences were observed between the CH predictions of the three mechanisms. These differences are consistent with the analysis carried out in Appendix B. The GRIMech 3.0 mechanism produces a peak CH concentration higher by a factor of about 2.4 than that from the AramcoMech 1.4 mechanism, while the modifications to this last mechanism increase the maximum CH mole fraction by a factor of 1.5. These differences propagate to the $i-V$ curves, with saturation currents from GRIMech 3.0 and Modified AramcoMech 1.4 mechanisms higher by factors of 2.3 and 1.3, respectively, than predicted by the original AramcoMech 1.4. These observations point out the proportionality between the saturation current and the peak value of CH concentration.

It should be noted that, for the richest flames ($\Phi \geq 1.3$), the CH predictions by various models are comparable and saturation currents may be more sensitive to differences in the O predictions. Thus, the optimization of O chemistry may improve the simulation of ions at rich conditions further. However, quantitative and comprehensive

measurements of O concentrations are scarce in the literature [64–66], making this task a challenging one.

5.1.2. On the role of chemi-ionization rate

All results presented above were obtained using the most recent rate constant available in the UMIST database [19] for the chemi-ionization reaction (R1):

$$k_{c,1} = 6.564 \times 10^{12} \left(\frac{T}{300}\right)^{-2.19} \exp\left(\frac{-327.9}{RT}\right),$$

where T is the temperature and units are cm, mol, s, cal, and K. In order to investigate the effect of the chemi-ionization rate on the $i{-}V$ curves, simulations with two additional sets of rate parameters available in the literature were performed. The first rate constant is from Ref. [62] and has been used in most previous modeling studies [3,8,42]:

$$k_{c,2} = 2.512 \times 10^{11} \exp\left(\frac{-1700}{RT}\right).$$

The second rate uses a modified value for the pre-exponential factor compared to $k_{c,2}$:

$$k_{c,3} = 1.031 \times 10^{11} \exp\left(\frac{-1700}{RT}\right).$$

The pre-exponential factor in $k_{c,3}$ has been proposed by Speelman et al. [4].

A comparison of the three rate constants is shown in Fig. 6. A discrepancy exists for the temperature dependence of the three rate constants. While $k_{c,1}$ increases with decreasing temperature, the other two rates are decreasing functions of temperature. Fig. 6 also highlights the range of temperatures relevant to chemi-ionization in the *HFB flame* at $\Phi = 1$ ($T \approx 1200 - 1900$ K) and temperature at which $k_{c,1}$ and $k_{c,2}$ are equal (T $\approx$ 1620 K). It is noted that the values of the three rates in the flame reaction zone are much lower than the estimate of $k_c = 1.8{\times}10^{12}$ ($\mathrm{cm^3{\cdot}mol^{-1}{\cdot}s^{-1}}$) from the early work of Green and Sugden [14].

Figure 7 displays the $i{-}V$ curves obtained with the three chemi-ionization rate constants in the *HFB flame* at $\Phi = 1$. Despite the differences between $k_{c,1}$ and $k_{c,2}$, the values of the saturation currents are comparable. This is because $k_{c,1}$ and $k_{c,2}$ are somewhat similar in the flame zone where charged species are produced ($T \approx 1200 - 1900$ K). The maximum ion production rate is obtained at 1780 K, where the ratio between $k_{c,2}$ and $k_{c,1}$ is approximatively 1.3, and equal to the ratio between the saturation currents. Not surprisingly, the saturation current is very sensitive to the value of the chemi-ionization rate constant at the flame location where the product of the CH and O concentrations peaks.

The simulated saturation currents at various equivalence ratios obtained with the three chemi-ionization rates are compared to the experimental values in Fig. 8. The chemi-ionization rate proposed by Speelman et al. [4] ($k_{c,3}$) significantly underestimates the saturation currents. This was expected since this rate was optimized based on simulations with the GRIMech 3.0 mechanism, which over-predicts the CH concentrations as shown in Appendix B. The importance of the CH predictions for the evaluation of ion kinetic data is clear and consistent with the authors' detailed analysis

of ion chemistry in combustible mixtures based on the uncertainty quantification in Ref. [18]. As the relation between the saturation current and the chemi-ionization rate constant is linear, it is concluded that the relatively high value proposed by Green and Sugden [14] (see Fig. 6) is inappropriate.

Predictions with $k_{c,1}$ and $k_{c,2}$ are equivalent, with $k_{c,2}$ providing a slightly better agreement with experiments. The differences between results from the two rates are minor for all equivalence ratios in the *McK flame* and stoichiometries lower than $\Phi = 1.0$ in the *HFB flame*. In these cases, the maximum ion production rate occurs at temperature where the values of $k_{c,1}$ and $k_{c,2}$ are nearly the same. For the rich equivalence ratios in the *HFB flame*, differences between saturation currents from $k_{c,1}$ and $k_{c,2}$ are more important because the differences between $k_{c,1}$ and $k_{c,2}$, at the temperature where the peak ion production rate is obtained, are more pronounced.

5.2. Saturation voltages

Because the intensity of the induced electric field depends on the concentration of charged species in the flame, the saturation voltage is also controlled by the amount of CH in the flame and chemi-ionization rate constant, and varies proportionally with the saturation current [27]. The analysis in Ref. [4] points out the importance of the transport coefficients of charged species and recombination reactions for the computation of the saturation voltage. An analysis of the role of the recombination reactions and ion transport is thus required to conclusively assess the model's performance.

5.2.1. On the role of recombination reactions

Equation 19 provides an expression for the current density drawn from the flame as a function of the saturation current and overall recombination. It shows clearly that the current decreases as the recombination increases. In other words, the higher the recombination, the higher the voltage bias needed to achieve saturation. The recombination is related to the concentration of H_3O^+ ion and electrons and recombination rate constant. The sensitivity of currents to the recombination rate constant is explored in this section.

As mentioned in Section 4, four recombination reactions were considered (R3a to R3d). All results presented previously were obtained using the most recent rate constants available in the UMIST database [19] for the four reactions (see Appendix A). The overall rate constant for recombination from the UMIST database was obtained by summing the four channels:

$$k_{r,UMIST} = 4.539 \times 10^{18} T^{-0.5},$$

where units are cm, mol, s, cal, and K. To evaluate the accuracy of the recombination rate constant, $i{-}V$ curves for three equivalence ratios ($\Phi = 0.8$, 1.0 and 1.2) measured in the *HFB flame* were simulated by using three additional rate constants available in the literature. The first rate was obtained by fitting the sum of the four rate constants used in Ref. [8]:

$$k_{r,Prager} = 9.332 \times 10^{20} T^{-0.964},$$

and the second rate was determined experimentally by Peeters et al. [63] based on

measurements of ion profiles in methane flames:

$$k_{r,Peeters} = 1.144 \times 10^{17}.$$

The last rate was proposed by Jones et al. [16] based on measurements of the concentrations of positive and negative ions in premixed rich flames of methane/oxygen:

$$k_{r,Jones} = 1.746 \times 10^{17}.$$

Figure 9 compares the four recombination rate constants. Both $k_{r,2}$ and $k_{r,1}$ are decreasing functions of temperature, while $k_{r,3}$ and $k_{r,4}$ are constant. Large differences exist between the values of $k_{r,1}$ and those of the other rate constants. For example, the ratio between $k_{r,2}$ and $k_{r,1}$ lies between 14 in the fresh gas region and 6 in the burnt gas region. Note that the values of the recombination rate constants at high temperatures, which are characteristic of the burnt region of a premixed flame where recombination occurs, are most relevant. In Fig. 10, the $i-V$ curves obtained with the four recombination rates are displayed for various equivalence ratios. It is clear that the use of $k_{r,2}$ is inappropriate.

The $i-V$ curve for positive bias voltages is much more sensitive to variations in the recombination rates than for negative voltages. The saturation voltage increases as the recombination rate constant increases. For negative voltages, the value of the recombination rate constant has a modest effect on the saturation voltage. At and above saturation, recombination does not occur since the charged species are removed from the flame, and thus the recombination rate constant does not have any effect.

Simulations using various recombination rate constants were also performed for the *McK flame* with three separation-distances: $L = 3.7$, 10 and 20 mm, respectively. As shown in Fig. 11, conclusions drawn from the simulations with the *HBF flame* also apply here for $L = 10$ and 20 mm, i.e. by increasing the recombination rate constant, the positive saturation voltage increases while the negative one is unchanged. For the smallest separation distance ($L = 3.7$ mm), the effect of the recombination rate constant on the i-V curve slope is insignificant in both polarities. As the distance between the flame surface and downstream electrode is decreased, higher electric strengths are induced and the charged species are removed rapidly in opposite directions. The recombination rate constant has thus a less significant effect on the i-V curve in this case given that the recombination process takes place only in zones where positive ions and electrons coexist.

5.2.2. On the role of transport

It is apparent from all $i-V$ curves shown so far, that a significant degree of asymmetry exists between positive and negative voltages. While the saturation currents are the same for both polarities, the current increases at a slower rate with negative polarity compared to a positive polarity, and higher negative voltages are required to achieve saturation conditions. These observations reflect the important role of the mobilities of negative and positive charges in controlling saturation voltages as highlighted by the recent works of Speelman et al. [4] and Han et al. [27]. It was found that, for a given burner-stabilized flame, the predicted saturation voltage is inversely proportional to the square of the electron mobility in the burnt gas for positive polarity, while it is inversely proportional to the square of the positive ion mobility in the burnt gas when a negative bias voltage is applied.

In the modeling framework adopted for ion diffusivity and mobility, model parameters are related to the polarizability of the species pair via semi-empirical formulas [38]. For each species, several polarizability values are available in the NIST CCCBDB [67] with an uncertainty estimated at 40% for most hydrocarbon species. In our simulations, results were obtained using the mean value of each species' polarizability $\bar{\alpha}$, which was calculated as the average of all the values provided in the database. The uncertainty of the ion transport was studied by varying the mean polarizabilies of species H_3O^+ and N_2 by as much as 40%. These species are chosen because they were the most abundant ion and neutral species in the flames considered here.

Figure 12 shows the $i-V$ curves and distribution of the mobility of H_3O^+ across the *HFB flame* with $\Phi = 1$, when $\bar{\alpha}_{H_3O^+}$ and $\bar{\alpha}_{N_2}$ are varied by $\pm$ 40% individually or simultaneously. When the polarizability of N_2 or H_3O^+ is increased, the mobility of ions decreases, and vice versa. Although the mobility of H_3O^+ was varied by as much as 24% as a result of simultaneously decreasing the polarazibilities by 40%, the saturation voltage was only slightly changed in the case of a positive bias. For negative voltages, the saturation voltage increases with increasing polarizability, and is inversely proportional to the mobility of H_3O^+. This observation holds when the polarizability of the other main neutral species (CH_4 or O_2) is also changed (not shown). The saturation voltage is more sensitive to the change in the polarizability of N_2, which is the most abundant species in the flame.

In our model, the electron mobility was computed as a function of temperature and gas mixture composition according to the methodology in Ref. [40]. The electron mobility decreases through the reaction zone and varies between 0.2 and 0.8 $m^2 \cdot V^{-1} \cdot s^{-1}$ in the flames simulated in this work. The influence of the electron mobility on the $i-V$ curves was studied by multiplying their local values by a factor of 0.2, 0.5, 2 or 5. The impact of using a constant electron mobility value ($\mu_e = 0.4$ $m^2 \cdot V^{-1} \cdot s^{-1}$), which is recommended for thermal electrons in gas burnt region of a stoichiometric methane/air flame [40], was also explored.

The influence of the electron mobility on the $i-V$ curves is shown in Fig. 13. For negative voltages, the $i-V$ profiles are not affected by the electron mobility and the saturation voltage is less sensitive to the details of the electron transport. For positive voltages, the saturation voltage is inversely proportional to the electron mobility. Currents obtained with a constant value for the electron mobility ($\mu_e = 0.4$ $m^2 \cdot V^{-1} \cdot s^{-1}$) coincide with the results obtained with a variable electron mobility, confirming the dependence of i-V curves on the value of electron mobility in the burnt gas.

6. Conclusions

A detailed modeling framework was proposed to predict $i-V$ curves in burner-stabilized premixed flames. An ion chemistry model [8] was applied to compute the fluxes of charged species. Rate constants of ion reactions and thermodynamic data of charged species were updated according to the most recent data in the UMIST [19] and Burcat [51] databases, respectively. The combustion of neutral species was represented by the detailed AramcoMech 1.4 mechanism [58,59], modified to improve CH prediction; this improvement was motivated by the important role of CH in the production of charges in flames.

The proposed model provides reasonable agreement with experimental data for the i-V curves. An implication of using the detailed AramcoMech 1.4 mechanism is that $i-V$ curves can be investigated for a comprehensive set of C1-C4 fuels over a wide range

of pressures, temperatures and stoichiometries. More experimental data, covering subsaturation and saturation regimes with negative voltages, are required to conclusively assess the performance of the ion transport model in predicting saturation voltages. Experimental measurements and numerical simulations of $i-V$ curves in lean-to-rich, atmospheric pressure flames of methane, ethane, propane, and n-butane with both positive and negative bias voltages are ongoing and will be reported at a later date.

Acknowledgement

This work was supported by competitive research funding provided by King Abdullah University of Science and Technology (KAUST).

References

[1] P. Mehresh, J. Souder, D. Flowers, U. Riedel, and R.W. Dibble, Combustion timing in HCCI engines determined by ion-sensor: experimental and kinetic modeling, Proc. Combust. Inst. 30 (2005), pp. 2701–2709.

[2] C. Daniel, V. Borrero, M. de la Cruz, S. Belhalfaoui, D. Thevenin, and F. Lacas, Analyse de la répartition du potentiel électrique dans les flammes, Proc. Acad. Sci. Series IIB - Mechanics 329 (2001), pp. 53–59.

[3] N. Speelman, M. Kiefer, D. Markus, U. Maas, L.P.H. de Goey, and J.A. van Oijen, Validation of a novel numerical model for the electric currents in burner-stabilized methane air flames, Proc. Combust. Inst. 35 (2014), pp. 847–854.

[4] N. Speelman, L.P.H. de Goey, and J.A. van Oijen, Development of a numerical model for the electric current in burner stabilized methane-air flames, Combust. Theor. Model. 19 (2015), pp. 159–187.

[5] S.M. Lee, C.S. Park, M.S. Cha, and S.H. Chung, Effect of electric fields on the liftoff of nonpremixed turbulent jet flames, IEEE Trans. Plasma. Sci. 33 (2005), pp. 1703–1709.

[6] L.B.W. Peerlings, M. Manohar, V.N. Kornilov, and L.P.H. de Goey, Flame ion generation rate as a measure of the flame thermo-acoustic response, Combust. Flame 160 (2013), pp. 2490–2496.

[7] M. Saito, T. Arai, and M. Arai, Control of soot emitted from acetylene diffusion flames by applying an electric field, Combust. Flame 119 (1999), pp. 356–366.

[8] J. Prager, U. Riedel, and J. Warnatz, Modeling ion chemistry and charged species diffusion in lean methane-oxygen flames, Proc. Combust. Inst. 31 (2007), pp. 1129–1137.

[9] M. Belhi, P. Domingo, and P. Vervisch, Modelling of the effect of DC and AC electric fields on the stability of a lifted diffusion methane/air flame, Combust. Theor. Model. 17 (2013), pp. 749–787.

[10] H. Calcote, Ion production and recombination in flames, Symp. (Int.) Combust. 8 (1961), pp. 184–199.

[11] G. Wortberg, Ion-concentration measurements in a flat flame at atmospheric pressure, Symp. (Int.) Combust. 10 (1965), pp. 651–655.

[12] A.B. Fialkov, Investigations on ions in flames, Prog. Energy Combust. Sci. 23 (1997), pp. 399–528.

[13] H. Calcote and J. Reuter, Mass-spectrometric study of ion profiles in low-pressure flames, J. Chem. Phys. 38 (1963), pp. 310–317.

[14] J. Green and T. Sugden, Some observations on the mechanism of ionization in flames containing hydrocarbons, Symp. (Int.) Combust. 9 (1963), pp. 607–621.

[15] J. Goodings, D. Bohme, and Chun-Wai Ng, Detailed ion chemistry in methane-oxygen flames. II. negative ions, Combust. Flame 36 (1979), pp. 45–62.

[16] Howard R.N. Jones and Allan N. Hayhurst, Measurements of the concentrations of positive and negative ions along premixed fuel-rich flames of methane and oxygen, Combust. Flame 166 (2016), pp. 86–97.

[17] S.D.T. Axford and A.N. Hayhurst, Mass spectrometric sampling of negative ions from flames of hydrogen and oxygen: The kinetics of electron attachment and detachment in hot mixtures of h_2o, o_2, oh and ho_2, Proc. Roy. Soc. (Lond) 452A (1996), pp. 1007–1033.

[18] D. Kim, F. Rizzi, K.W. Cheng, J. Han, F. Bisetti, and O.M. Knio, Uncertainty quantification of ion chemistry in lean and stoichiometric homogenous mixtures of methane, oxygen, and argon, Combust. Flame 162 (2015), pp. 2904–2915.

[19] D. McElroy, C. Walsh, A.J. Markwick, M.A. Cordiner, K. Smith, and T.J. Millar, The UMIST database for astrochemistry 2012, A&A 550 (2013), pp. 1–13.

[20] C. Butler and A. Hayhurst, Measurement of the maximum concentration of ch radicals from observations of ionic abundances in a flame, Proc. Anglo-German Combust. Symp. British Section of the Combustion Institute, Cambridge (1993), pp. 180–183.

[21] P. Versailles, G.M. Watson, A.C. Lipardi, and J.M. Bergthorson, Quantitative CH measurements in atmospheric-pressure, premixed flames of C1-C4 alkanes, Combust.

Flame 165 (2016), pp. 109–124.
[22] John W. Thoman Jr. and A. McIlroy, Absolute CH radical concentrations in rich low-pressure methane-oxygen-argon flames via cavity ringdown spectroscopy of the $A^2\Delta$-$X^2\Pi$ transition, J. Phys. Chem. A 104 (2000), pp. 4953–4961.
[23] P.A. Berg, D.A. Hill, A.R. Noble, G.P. Smith, J.B. Jeffries, and D.R. Crosley, Absolute CH concentration measurements in low-pressure methane flames: Comparisons with model results, Combust. Flame 121 (2000), pp. 223–235.
[24] J. Lawton and F.J. Weinberg, Maximum ion currents from flames and the maximum practical effects of applied electric fields, Proc. Roy. Soc. A (Lond) 277 (1963), pp. 468–497.
[25] J. Lawton and F.J. Weinberg, Electrical aspects of combustion, Oxford University Press, 1970.
[26] J. Goodings, J. Guo, A. Hayhurst, and S. Taylor, Current-voltage characteristics in a flame plasma: analysis for positive and negative ions, with applications, Int. J. Mass. Spectrom. 206 (2001), pp. 137–151.
[27] J. Han, M. Belhi, T.A. Casey, F. Bisetti, H.G. Im, and J.Y. Chen, The $i - V$ curve characteristics of burner-stabilized premixed flames: detailed and reduced models, Proc. Combust. Inst. (2016), p. Accepted.
[28] N. Speelman, Model development for ionization phenomena in premixed laminar flames, Ph.D. diss., Eindhoven University of Technology, The Netherlands, 2015.
[29] R.J. Kee, A Fortran Program for Modeling Steady Laminar One-Dimensional Premixed Flames, Sandia National Laboratories, 1985.
[30] J. van den Boom, A. Konnov, A. Verhasselt, V. Kornilov, and L. de Goey, The effect of a dc electric field on the laminar burning velocity of premixed methane/air flames, Proc Comb. Inst. 32 (2009), pp. 1237–1244.
[31] M. Sanchez-Sanza, D. Murphy, and C. Fernandez-Pello, Effect of an external electric field on the propagation velocity of premixed flames, Proc Comb. Inst. 35 (2015), pp. 3463–3470.
[32] Holthuis & Associates, Mckenna flat flame burner, PO Box 1531, Sebastopol, CA 95473, USA, http://www.flatflame.com .
[33] K. Bosschaart, Analysis of the heat flux method for measuring burning velocities, Ph.D. diss., Eindhoven University of Technology, The Netherlands, 2002.
[34] E. Mason and E. McDaniel, Transport Properties of Ions in Gases, John Wiley & Sons, Inc., 1988.
[35] R.V.Chiflikian, The analog of blancs law for drift velocities of electrons in gas mixtures in weakly ionized plasma, Phys. Plasmas 2 (1995), pp. 3902–3909.
[36] W.F. Siems, L.A. Viehland, and J. Herbert H. Hill, Improved momentum-transfer theory for ion mobility. 1. derivation of the fundamental equation, Anal. Chem. 84 (2013), pp. 9782–9791.
[37] E. Mason, R. Munn, and J. Smith, Transport coefficients of ionized gases, Phys. Fluids 10 (1967), pp. 1827–1832.
[38] J. Han, M. Belhi, F. Bisetti, and S.M. Sarathy, Numerical modelling of ion transport in flames, Combust. Theor. Model. 19 (2015), pp. 744–772.
[39] F. Bisetti and M.E. Morsli, Kinetic parameters, collision rates, energy exchanges and transport coefficients of non-thermal electrons in premixed flames at sub-breakdown electric field strengths, Combust. Theor. Model. 18 (2014), pp. 148–184.
[40] F. Bisetti and M. El-Morsli, Calculation and analysis of the mobility and diffusion coefficient of thermal electrons in methane/air premixed flames, Combust. Flame 159 (2012), pp. 3518–3521.
[41] LXcat 2012, Phelps (N_2, CO), Morgan (O_2, H_2, CO_2, H_2O), and Hayashi (CH_4) databases, http://www.lxcat.laplace.univ-tlse.fr (2012).
[42] M. Belhi, P. Domingo, and P. Vervisch, Direct numerical simulation of the effect of an electric field on flame stability, Combust. Flame 157 (2010), pp. 2286–2297.
[43] S. Mahadevan and L.L. Raja, Simulations of direct-current air glow discharge at pressures

$\sim$ 1 torr: Discharge model validation, J. Appl. Phys. 107 (2010), pp. 1–11.
[44] T. Poinsot and D. Veynante, Theoretical and Numerical Combustion, 3rd ed., Aquaprint, Bordeaux, France, 2013.
[45] E. Volkov, V. Kornilo, and L. de Goey, Experimental evaluation of dc electric field effect on the thermoacoustic behaviour of flat premixed flames, Proc. Combust. Inst. 34 (2013), pp. 955–962.
[46] A. Patyal, D. Kyritsis, and M. Matalon, Electric field effects in the presence of chemi-ionization on droplet burning, Combust. Flame 164 (2016), pp. 99–110.
[47] D. Park, S. Chung, and M. Cha, Bidirectional ionic wind in nonpremixed counterflow flames with dc electric fields, Combust. Flame 168 (2016), pp. 138–146.
[48] A.R.D. Farraj, R. Rajasegar, A.N. Al-Khateeb, and D.C. Kyritsis, Phenomenology of electrostatically manipulated laminar counterflow non-premixed methane flames, J. Energy Eng. 142 (2016), p. E4015013.
[49] A.R.D. Farraj, A.M. AL-Naeemy, A.N. Al-Khateeb, and D.C. Kyritsis, Laminar non-premixed counterflow flames manipulation through the application of external direct current fields, J. Energy Eng. 143 (2017), p. 04017002.
[50] M. Papac and D. Dunn-Rankin, Modelling electric field driven convection in small combustion plasmas and surrounding gases, Combust. Theory Model. 12 (2007), pp. 23–44.
[51] A. Burcat, Prof. Burcat's thermodynamic data : Ideal gas thermodynamic data in polynomial form for combustion and air pollution use, http://garfield.chem.elte.hu/Burcat/burcat.html (2006).
[52] J. Goodings, D. Bohme, and Chun-Wai Ng, Detailed ion chemistry in methane-oxygen flames. I. positive ions, Combust. Flame 36 (1979), pp. 27–43.
[53] A.B. Alquaity, B. Chen, J. Han, H. Selim, M. Belhi, Y. Karakaya, T. Kasper, S.M. Sarathy, F. Bisetti, and A. Farooq, New insights into methane-oxygen ion chemistry, Proc. Combust. Inst. Accepted (2016).
[54] T. Pedersen and R.C. Brown, Simulation of electric field effects in premixed methane flames, Combust. Flame 94 (1993), pp. 433–448.
[55] A. Eraslan and R. Brown, Chemiionization and ion-molecule reactions in fuel-rich acetylene flames, Combust. Flame 74 (1988), pp. 19–37.
[56] K. Yamashita, S. Karnani, and D. Dunn-Rankin, Numerical prediction of ion current from a small methane jet flame, Combust. Flame 156 (2009), pp. 1227–1233.
[57] M. Belhi, B.J. Lee, F. Bisetti, and H.G. Im, A computational study of the effects of dc electric fields on non-premixed counterflow methane-air flames, Journal of Physics D: Applied Physics 10.1088/1361-6463/aa94bb (2017), Available at http://iopscience.iop.org/10.1088/1361-6463/aa94bb.
[58] S. Burke, W. Metcalfe, O. Herbinet, F. Battin-Leclerc, F. Haas, J. Santner, F. Dryer, and H. Curran, An experimental and modeling study of propene oxidation. part 1: speciation measurements in jet-stirred and flow reactors, Combust. Flame 161 (2014), pp. 2765–2784.
[59] S. Burke, U. Burke, R.M. Donagh, O. Mathieu, I. Osorio, C. Keesee, A. Morones, E. Petersen, W. Wang, T. DeVerter, M. Oehlschlaeger, B. Rhodes, R. Hanson, D. Davidson, B. Weber, C.J. Sung, J. Santner, Y. Ju, F. Haas, F. Dryer, E. Volkov, E. Nilsson, A. Konnov, M. Alrefae, F. Khaled, A. Farooq, P. Dirrenberger, P.A. Glaude, F. Battin-Leclerc, and H. Curran, An experimental and modeling study of propene oxidation. part 2: ignition delay time and flame speed measurements, Combust. Flame 162 (2015), pp. 296–314.
[60] G.P. Smith, D.M. Golden, M. Frenklach, N.W. Moriarty, B. Eiteneer, M. Goldenberg, C.T. Bowman, R.K. Hanson, S. Song, J. William C. Gardiner, V.V. Lissianski, and Z. Qin, GRI-Mech version 3.0 http://combustion.berkeley.edu/gri-mech/ (2000).
[61] R.J. Kee, M.E. Coltrin, and P. Glarborg, Chemically Reacting Flow: Theory & Practice, John Wiley & Sons, Inc, 2003.
[62] J. Warnatz, Combustion Chemistry, chap. Rate Coefficients in the C/H/O System, Springer-Verlag New York Inc. (1984), pp. 197–360.

[63] J. Peeters, C. Vinckier, and A.V. Tiggelen, Formation and behavior of chemi-ions in flames, Oxid. Combustion. Rev. 4 (1969), pp. 93–132.

[64] T.L. Chng and R.B. Miles, Absolute concentration measurements of atomic oxygen in a flame using radar rempi, AIAA SciTech Forum National Harbor, Maryland 52nd Aerospace Sciences Meeting (2014).

[65] U. Meier, J. Bittner, K. Kohse-Hinghaus, and T. Just, Discussion of two-photon laser-excited fluorescence as a method for quantitative detection of oxygen atoms in flames, Symp. (Int.) Combust. 22 (1989), pp. 1887–1896.

[66] J.H. Frank and T.B. Settersten, Two-photon lif imaging of atomic oxygen in flames with picosecond excitation, Proc Comb. Inst. 30 (2005), pp. 1527–1534.

[67] NIST Computational Chemistry Comparison and Benchmark Database, NIST Standard Reference Database Number 101 Release 17b, Sep. 2015, Editor: Russell D. Johnson III http://cccbdb.nist.gov/ .

[68] J. Brian and A. Mitchell, The dissociative recombination of molecular ions, Phys. Rep. 186 (1990), pp. 215–248.

[69] N. Adams, D. Smith, and D. Grief, Reactions of H_nCO^+ ions with molecules at 300 K, Int. J. Mass Spectr. Ion Phys. 26 (1978), pp. 405–415.

[70] O. Novotny, H. Buhr, J. Stutzel, M.B. Mendes, M.H. Berg, D. Bing, M. Froese, M. Grieser, B.J.T. Oded Heber, C. Krantz, M. Lange, M. Lestinsky, S. Novotny, S. Menk, D.A. Orlov, A. Petrignani, M.L. Rappaport, A. Shornikov, D. Schwalm, D. Zajfman, and A. Wolf, Fragmentation channels in dissociative electron recombination with hydronium and other astrophysically important species, J. Phys. Chem. A 114 (2010), pp. 4870–4874.

[71] M.J. Jensen, R.C. Bilodeau, C.P. Safvan, K. Seiersen, L.H. Andersen, H.B. Pedersen, and O. Heber, Dissociative recombination of H_3O^+, HD_2O^+, and D_3O^+, Astrophys. J. 543 (2000), pp. 764–774.

[72] S.S. Prasad and J. Huntress W. T., A model for gas phase chemistry in interstellar clouds. I - the basic model, library of chemical reactions, and chemistry among C, N, and O compounds, Astrophys. J. Suppl S. 43 (1980), pp. 1–35.

[73] S.D.T. D. K. Bohme G. I. Mackay, An experimental study of the gas-phase kinetics of reactions with hydrated hydronium(1+) ions(n = 1-3) at 298 K, J. Am. Chem. Soc. 101 (1979), pp. 3724–3730.

[74] S. Tanner, G. Mackay, A. Hopkinson, and D. Bohme, Proton transfer reactions of HCO^+ at 298 K, Int. J. Mass Spectr. Ion Phys. 29 (1979), pp. 153–169.

[75] V.G. Anicich, Evaluated bimolecular ion-molecule gas phase kinetics of positive ions for use in modeling planetary atmospheres, cometary comae, and interstellar clouds, J. Phys. Chem. Ref. Data 22 (1993).

[76] W.D. Geppert, M. Hamberg, R.D. Thomas, F. Osterdahl, F. Hellberg, V. Zhaunerchyk, A. Ehlerding, T.J. Millar, H. Roberts, J. Semaniak, M. af Ugglas, A. Kallberg, A. Simonsson, M. Kaminskad, and M. Larssona, Dissociative recombination of protonated methanol, Faraday Discuss. 133 (2006), pp. 170–190.

[77] E.E. Ferguson, Rate constants of thermal energy binary ion-molecule reactions of aeronomic interest, Atom. Data Nucl. Data 12 (1973), pp. 159–178.

[78] A. Starik, A. Savelev, N. Titova, and U. Schuhmann, Modeling of sulfur gases and chemiions in aircraft engines, Aero. Sci. Tech. 6 (2002), pp. 63–81.

[79] V.G. Anicich, An index of the literature for bimolecular gas phase cation-molecule reaction kinetics, JPL Publication 03-19, 2003.

[80] Y.H.L. Teuff, T.J. Millar, and A.J. Markwick, The umist database for astrochemistry 1999, Astron. Astrophys. Suppl. Ser. 146 (2000), pp. 157–168.

[81] R. Brown and A. Eraslan, Simulation of ionic structure in lean and close-to-stoichiometric acetylene flames, Combust. Flame 73 (1988), pp. 1–21.

[82] S.M. Starikovskaia, A.Y. Starikovskii, and D.V. Zatsepin, Hydrogen oxidation in a stoichiometric hydrogen-air mixture in the fast ionization wave, Combust. Theory Model. 5 (2001), pp. 97–129.

[83] A.N. Hayhurst, The mass spectrometric sampling of ions from atmospheric pressure flames

as exemplified by the reactions of OH and O_2^- in O_2-rich flames, Pure Appl. Chem. 65 (1993), pp. 285–295.

[84] M. Capitelli, C.M. Ferreira, B.F. Gordiets, and A.I. Osipov, Plasma Kinetics in Atmospheric Gases, Springer, New York, 2000.

[85] D. Bohme, J. Goodings, and Chun-Wai Ng, In situ chemical ionization as a probe for neutral constituents upstream in a methane-oxygen flame, Int. J. Mass Spectr. Ion Phys. 24 (1977), pp. 335–354.

[86] Reaction Design, Chemkin-pro release 15131, 2013 .

[87] S. Zabarnick, J.W. Fleming, and M.C. Lin, Kinetic study of the reaction $CH(X^2\Pi) + H_2 \rightleftharpoons CH_2(X^3B_1) + H$ in the temperature range 372 to 675 K, J. Chem. Phys. 85 (1986), pp. 4373–4376.

[88] C.T. Bowman, R.K. Hanson, D.F. Davidson, W.C. Gardiner Jr., V. Lissianski, G.P. Smith, D.M. Golden, M. Frenklach, and M. Goldenberg, GRI-Mech version 2.11 http://combustion.berkeley.edu/gri-mech/.

[89] A. Bergeat, S. Moisan, R. Mreau, and J.C. Loison, Kinetics and mechanisms of the reaction of CH with H_2O, Chem. Phys. Lett. 480 (2009), pp. 21–25.

[90] P. Glarborg, J.A. Miller, and R.J. Kee, Western States Section, San Antonio (1985) .

[91] K. Devriendt, M. Van Poppel, W. Boullart, and J. Peeters, Kinetic investigation of the $CH_2(X^3B_1) \rightarrow H + CH(X^2\Pi) + H_2$ reaction in the temperature range 400 K $< T <$ 1000 K, J. Phys. Chem. 99 (1995), pp. 16953–16959.

[92] D. Baulch, C. Cobos, R. Cox, C. Esser, P. Frank, T. Just, J. Kerr, M. Pilling, J. Troe, R. Walker, and J. Warnatz, Evaluated kinetic data for combustion modeling, J. Phys. Chem. 21 (1992), pp. 411–429.

Appendix A. Reaction mechanism of charged species

Reaction	A ($cm^3 \cdot mol^{-1} \cdot s^{-1}$ or $cm^6 \cdot mol^{-1} \cdot s^{-1}$)	n	E_a ($cal \cdot mol^{-1}$)	Ref.
Reactions in Prager et al. [8] for which the rate parameters have been updated based on the most recent data in the UMIST database [19]:				
$CH + O \rightleftharpoons HCO^+ + e^-$	1.746×10^{18}	-2.19	327.889	[19]
$HCO^+ + e^- \rightleftharpoons CO + H$	7.399×10^{18}	-0.69	0	[68]
$HCO^+ + H_2O \rightleftharpoons H_3O^+ + CO$	2.608×10^{16}	-0.5	0	[69]
$H_3O^+ + e^- \rightleftharpoons H_2O + H$	7.395×10^{17}	-0.5	0	[70]
$H_3O^+ + e^- \rightleftharpoons OH + H + H$	3.181×10^{18}	-0.5	0	[70]
$H_3O^+ + e^- \rightleftharpoons H_2 + OH$	5.601×10^{17}	-0.5	0	[70]
$H_3O^+ + e^- \rightleftharpoons O + H_2 + H$	5.841×10^{16}	-0.5	0	[71]
$H_3O^+ + C \rightleftharpoons HCO^+ + H_2$	6.022×10^{11}	0	0	[72]
$C_2H_3O^+ + e^- \rightleftharpoons CH_2CO + H$	3.129×10^{18}	-0.5	0	[19]
$H_3O^+ + CH_2CO \rightleftharpoons C_2H_3O^+ + H_2O$	2.086×10^{16}	-0.5	0	[73]
$C_2H_3O^+ + e^- \rightleftharpoons CO + CH_3$	3.129×10^{18}	-0.5	0	[72]
$HCO^+ + CH_3OH \rightleftharpoons CH_5O^+ + CO$	2.816×10^{16}	-0.5	0	[74]
$H_3O^+ + CH_3OH \rightleftharpoons CH_5O^+ + H_2O$	2.608×10^{15}	-0.5	0	[75]
$CH_5O^+ + e^- \rightleftharpoons CH_3OH + H$	4.653×10^{16}	-0.59	0	[76]
$OH^- + H \rightleftharpoons H_2O + e^-$	8.431×10^{14}	0	0	[77]
$OH^- + C \rightleftharpoons HCO + e^-$	3.011×10^{14}	0	0	[72]
$OH^- + CH \rightleftharpoons CH_2O + e^-$	3.011×10^{14}	0	0	[72]
$OH^- + CH_3 \rightleftharpoons CH_3OH + e^-$	6.022×10^{14}	0	0	[72]
$O^- + C \rightleftharpoons CO + e^-$	3.011×10^{14}	0	0	[72]
$O^- + H_2 \rightleftharpoons OH^- + H$	1.807×10^{13}	0	0	[77]
$O^- + CH_4 \rightleftharpoons OH^- + CH_3$	6.022×10^{12}	0	0	[77]
$O^- + C_2H_6 \rightleftharpoons C_2H_5 + OH^-$	6.130×10^{15}	-0.5	0	[78]
$O^- + H \rightleftharpoons OH + e^-$	3.011×10^{14}	0	0	[72]
$O^- + H_2 \rightleftharpoons H_2O + e^-$	4.215×10^{14}	0	0	[77]
$O^- + CH \rightleftharpoons HCO + e^-$	3.011×10^{14}	0	0	[72]
$O^- + CH_2 \rightleftharpoons CH_2O + e^-$	3.011×10^{14}	0	0	[72]
$O^- + CO \rightleftharpoons CO_2 + e^-$	3.914×10^{14}	0	0	[77]
$O^- + O \rightleftharpoons O_2 + e^-$	1.144×10^{14}	0	0	[77]
Reactions in Prager et al. [8] for which the rate parameters are as they appear in Ref. [8]:				
$HCO^+ + C_2H_5OH \rightleftharpoons H_3O^+ + CO + C_2H_4$	6.000×10^{13}	0	0	[79]
$HCO^+ + CH_2CO \rightleftharpoons C_2H_3O^+ + CO$	1.259×10^{14}	-0.048	0	[80]
$HCO^+ + CH_3 \rightleftharpoons C_2H_3O^+ + H$	7.763×10^{14}	-0.006	0	[81]
$C_2H_3O^+ + O \rightleftharpoons HCO^+ + CH_2O$	2.000×10^{14}	0	0	[8]
$CH_5O^+ + CH_2CO \rightleftharpoons C_2H_3O^+ + CH_3OH$	1.486×10^{15}	-0.077	-82.93	[8]
$O_2^- + H_2 \rightleftharpoons H_2O_2 + e^-$	6.022×10^{14}	0	0	[8]
$O_2^- + H \rightleftharpoons HO_2 + e^-$	7.226×10^{14}	0	0	[82]
$O_2^- + OH \rightleftharpoons OH^- + O_2$	6.022×10^{13}	0	0	[83]
$O_2^- + H \rightleftharpoons OH^- + O$	1.084×10^{15}	0	0	[82]
$OH^- + O \rightleftharpoons HO_2 + e^-$	1.204×10^{14}	0	0	[15]
$CO_3^- + H \rightleftharpoons OH^- + CO_2$	1.020×10^{14}	0	0	[15]
$CO_3^- + O \rightleftharpoons O_2^- + CO_2$	4.600×10^{13}	0	0	[15]
$CHO_2^- + H \rightleftharpoons CO_2 + H_2 + e^-$	1.159×10^{14}	0	0	[8]
$OH^- + HCO \rightleftharpoons CHO_2^- + H$	2.959×10^{15}	-0.14	-105.3	[8]
$O^- + H_2O \rightleftharpoons OH^- + OH$	8.431×10^{14}	0	0	[84]
$O^- + CH_2O \rightleftharpoons OH^- + HCO$	5.601×10^{14}	0	0	[85]
$O^- + CH_2O \rightleftharpoons CHO_2^- + H$	1.307×10^{15}	0	0	[85]
$O^- + C_2H_2 \rightleftharpoons CH_2CO + e^-$	7.226×10^{14}	0	0	[85]
$O^- + H_2O \rightleftharpoons H_2O_2 + e^-$	3.613×10^{19}	0	0	[82]

$O_2^- + O \rightleftharpoons O^- + O_2$	1.987×10^{14}	0	0	[84]
$O_2^- + C_2H_3O^+ \rightleftharpoons O_2 + CH_3CO$	2.090×10^{18}	-0.5	0	[78]
$O_2^- + C_2H_3O^+ \rightleftharpoons O_2 + CH_2CO + H$	1.000×10^{18}	0	0	[8]
$O_2^- + CH_5O^+ \rightleftharpoons O_2 + CH_3 + H_2O$	1.000×10^{18}	0	0	[8]
$O^- + C_2H_3O^+ \rightleftharpoons O + CH_3CO$	2.090×10^{18}	-0.5	0	[78]
$O^- + C_2H_3O^+ \rightleftharpoons O + CH_2CO + H$	1.000×10^{18}	0	0	[8]
$O^- + C_2H_3O^+ \rightleftharpoons O + CH_2CHO$	1.000×10^{18}	0	0	[8]
$O^- + CH_5O^+ \rightleftharpoons O + CH_3 + H_2O$	1.000×10^{18}	0	0	[8]
$CHO_3^- + C_2H_3O^+ \rightleftharpoons CH_3CO + CO_2 + OH$	2.000×10^{18}	0	0	[8]
$CHO_3^- + CH_5O^+ \rightleftharpoons CH_3OH + H_2O + CO_2$	2.000×10^{18}	0	0	[8]
$O_2 + e^- + O \rightleftharpoons O_2^- + O$	3.627×10^{16}	0	0	[84]
$O_2 + e^- + O_2 \rightleftharpoons O_2^- + O_2$	1.523×10^{21}	-1	1191.9	[84]
$O_2 + e^- + H_2O \rightleftharpoons O_2^- + H_2O$	5.077×10^{18}	0	0	[84]
$O_2 + e^- + N_2 \rightleftharpoons O_2^- + N_2$	3.590×10^{21}	-2	139	[84]
$e^- + OH + H_2 \rightleftharpoons OH^- + H_2$	1.088×10^{17}	0	0	[83]
$e^- + OH + H_2O \rightleftharpoons OH^- + H_2O$	7.072×10^{17}	0	0	[83]
$e^- + OH + O_2 \rightleftharpoons OH^- + O_2$	4.352×10^{16}	0	0	[83]
$e^- + OH + N_2 \rightleftharpoons OH^- + N_2$	4.352×10^{16}	0	0	[83]
$e^- + OH + CO \rightleftharpoons OH^- + CO$	8.160×10^{16}	0	0	[83]
$e^- + OH + CO_2 \rightleftharpoons OH^- + CO_2$	1.632×10^{17}	0	0	[83]
$e^- + OH + CH_4 \rightleftharpoons OH^- + CH_4$	3.264×10^{17}	0	0	[83]
$OH^- + CO_2 + O_2 \rightleftharpoons CHO_3^- + O_2$	2.760×10^{20}	0	0	[15]
$OH^- + CO_2 + H_2O \rightleftharpoons CHO_3^- + H_2O$	1.104×10^{21}	0	0	[8]
$e^- + O + O_2 \rightleftharpoons O^- + O_2$	3.627×10^{16}	0	0	[84]
$e^- + O + O \rightleftharpoons O^- + O$	3.021×10^{17}	0	0	[82]
$O^- + CO_2 + O_2 \rightleftharpoons CO_3^- + O_2$	1.123×10^{21}	0	0	[15]

Appendix B. Optimization of CH chemistry

In this Appendix, the optimization process of CH chemistry is presented. CH predictions are compared to the experimental measurements presented in Versaille et al. [21], Thoman et al. [22] and Berg al. [23], respectively. These studies were chosen because detailed measured profiles of the absolute CH mole fractions and temperature were provided for a wide range of conditions.

Comparison to the experiment of Versaille et al. [21]

Figure B.1 compares the peak CH mole fractions predicted adopting AramcoMech 1.4 and GRIMech 3.0 mechanisms against the experimental measurements of Versailles et al. [21]. In the experiment, CH concentrations were obtained from 2D Planar Laser-Induced Fluorescence (PLIF) measurements for atmospheric-pressure, premixed, jet-wall stagnation flames of methane, ethane, propane, or n-butane, at equivalence ratios ranging from 0.7 to 1.5. Predictions of CH mole fractions in the present work are obtained using the Chemkin-Pro software [86] for premixed laminar stagnation flames.

The combustion of n-butane species cannot be simulated using the GRIMech 3.0 mechanism since this compound is not in the mechanism. For the other fuels, the GRIMech 3.0 mechanism overestimates the peak CH mole fractions. The overestimation is higher than the upper uncertainty bound in the experimental data in most cases. The AramcoMech 1.4 mechanism provides a better prediction of CH peak mole fractions compared to the GRIMech 3.0 model, even though the differences between computed and measured values exceed the experimental uncertainty in most cases.

By examining the reaction pathways of CH in the AramcoMech 1.4 mechanism, it was found that: (1) the main route for CH formation is : $CH_3 \longrightarrow CH_2(S) \longrightarrow CH_2 \longrightarrow CH$, and (2) CH is mainly consumed to form C, H or O atoms. The most

important source of CH production from CH_2 is the reaction:

$$CH_2 + H \rightleftharpoons CH + H_2. \quad \text{(B.R1)}$$

The contribution of reaction B.R1 to CH formation in the flames studied here varies between 50% and 70% depending on the equivalence ratio and fuel. On the other hand, the reaction:

$$CH + H_2O \rightleftharpoons H + CH_2O \quad \text{(B.R2)}$$

is an important contributor to the CH consumption in rich flames. For equivalence ratios higher than 1.2, removing reaction B.R2 from the AramcoMech 1.4 mechanism may increase the CH concentration by 10 to 20%. These main channels are consistent with the reaction network in the GRIMech 3.0 mechanism and the analysis in Versailles et al. [21]. Modifying the rate constants of reactions B.R1 and B.R2 affects the mole fractions of CH significantly without influencing the main characteristics of combustion for the fuels considered.

Various values for the rate parameters of the first reaction (B.R1) are available in the literature, showing large differences and/or discrepancies in the temperature dependence (see Fig. 2(a)). There is also a disagreement over the rate constants used for the second reaction (B.R2) (see Fig. 2(b)). The rate constants suggested in Refs. [87] and [88] allow for the closest agreement between the simulations and experiments [21] and thus were adopted here. The first rate (B.R1) was determined experimentally by laser-induced fluorescence of CH radicals, while the second rate (B.R2) was estimated based on the optimization of the GRIMech 2.11 mechanism in order to predict NO formation adequately [88]. Reaction B.R2 plays an important role in prompt NO formation but does not have an effect on the carbon- oxygen-hydrogen chemistry of methane combustion [88]. The original and modified rate constant parameters for the two reactions are shown in Table B.1.

For the sake of clarity, the AramcoMech 1.4 mechanism including the above two rate modifications will be referred to as the Modified AramcoMech 1.4 mechanism. It should be noted that these modifications do not affect the concentrations of other major neutral species and the fundamental properties of combustion, such as flame speed and temperature for the fuels considered. However, altering the chemistry of CH may modify the predictions of minor species of interest, such as NOx [21,88]. As can be seen from Fig. B.1, the Modified AramcoMech 1.4 mechanism (red lines with triangles) provides the best predictions of CH, with peak mole fractions within the uncertainty interval in most cases.

Comparison to the experiment of Thoman et al. [22]

Model predictions are compared to experimental data from rich, low-pressure (31 Torr) methane/oxygen/argon flames [22]. Profiles of CH mole fraction are shown in Fig. B.3 for four equivalence ratios: 1.0, 1.2, 1.4, and 1.6. Calculations were performed using the premixed laminar burner stabilized flame module of the Chemkin-Pro software [86]. All simulations were run in the fixed gas temperature mode with temperatures and boundary conditions taken from the experiments.

Generally, good qualitative agreement between the three mechanisms and the data was found, with the Modified AramcoMech 1.4 mechanism showing the best agreement with experimental data for all equivalence ratios. The conclusions drawn from

comparison to the experiments of Versailles et al. [21] also apply here. The GRIMech 3.0 mechanism predicts a higher CH peak mole fraction and a wider CH profile than experimentally observed. The modifications to the AramcoMech 1.4 mechanism improve the CH predictions significantly in terms of the peak concentration as well as the profile width and position.

Comparison to the experiment of Berg al. [23]

In Fig. B.4, the model is evaluated against experimental CH concentration profiles for low-pressure (30-40 Torr), premixed, laminar CH_4/O_2 flames diluted with N_2. The flames were modeled as burner stabilized flames using temperature profiles measured experimentally. Measured and calculated CH concentration profiles are compared for three equivalence ratios: 0.81, 1.07 and 1.28. As for the previous comparisons, the agreement between measured concentrations and model predictions varies with the equivalence ratio. However, the closest agreement for all equivalence ratios is obtained with the GRIMech 3.0 model; this contradicts findings from comparisons to the experiments of Versailles et al. [21] and Thoman et al. [22]. In this case, although the modifications to the AramcoMech 1.4 mechanism improve the CH predictions, underprediction of the peak CH mole fraction is apparent.

Summary

While the mechanisms reproduce the evolution of the peak CH concentration with the equivalence ratio, quantitative differences remain. In addition, the degree of agreement when using any model varies with fuel, diluent, stoichiometry and pressure. From the comparisons shown above, it is clear that no one optimal mechanism exists for all three sets of experimental data. Nonetheless, it is apparent that the modifications to the AramcoMech 1.4 mechanism improve the CH predictions significantly and yields the best overall performance over the range of fuels, equivalence ratios and pressures investigated.

The modified AramcoMech 1.4 mechanism was optimized based on experiments in Ref. [21], which provide the most current and comprehensive measurements of CH in flames. In contrast to the burner stabilized flame configuration in Refs. [22,23], the stagnation flame configuration in Ref. [21] produced lifted flames accessible for optical diagnostics and free from influences of the burner boundaries, making them ideal for numerical simulations. As shown in Fig. 1(a), the results from the Modified AramcoMech 1.4 mechanism are in very good agreement with the experimental data for methane flames, where mixture properties, temperature and pressure conditions are similar to those of flames investigated by Speelman et al. [3,4]. Therefore, the Modified AramcoMech 1.4 was used in the simulation of the $i-V$ curves.

Polarity	$x = 0$	$x = L$
$\Delta V > 0$	$dY^+/dx = 0$, $Y^- = 0$	$Y^+ = 0$, $dY^-/dx = 0$
$\Delta V < 0$	$Y^+ = 0$, $dY^-/dx = 0$	$dY^+/dx = 0$, $Y^- = 0$

Table 1. Boundary conditions for the charged species.

	AramcoMech 1.4				Modified AramcoMech 1.4			
Reaction	A	n	E_a	Ref.	A	n	E_a	Ref.
B.R1: $CH_2 + H \rightleftharpoons CH + H_2$	3×10^{13}	–	–	[89]	2.830×10^{14}	–	735	[87]
B.R2: $CH + H_2O \rightleftharpoons H + CH_2O$	1.774×10^{16}	-1.22	24	[90]	1.713×10^{13}	–	-755	[88]

Table B.1. Modification to AramcoMech 1.4 mechanism [58,59] to improve CH predictions against experimental measurements [21]. A , n and E_a are the pre-exponential factor, temperature factor and energy of activation in the Arrhenius equation. Units are cm, mol, s and cal.

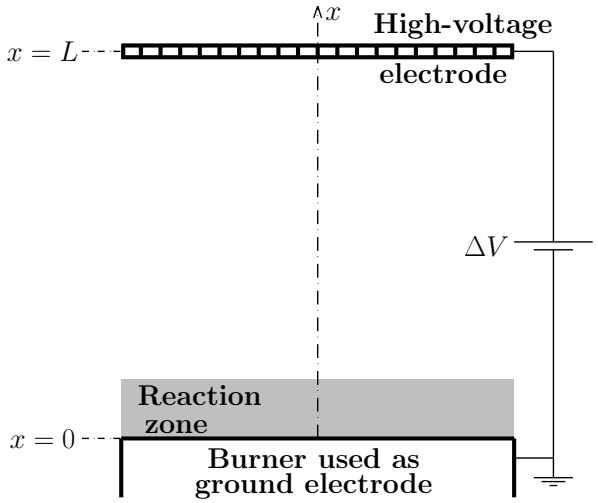

Figure 1. Numerical configuration inspired by experimental setup in Refs. [3,4].

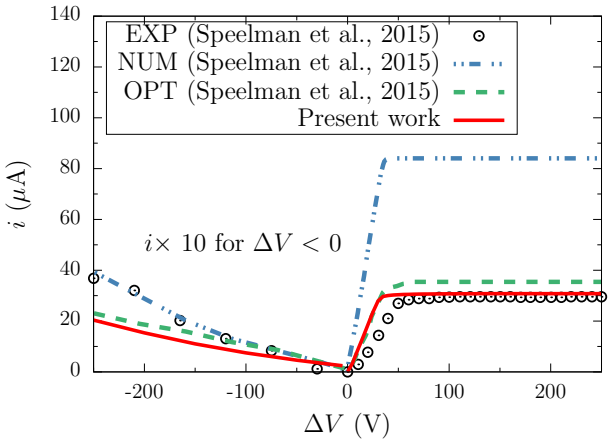

(a) $\Phi = 0.8$

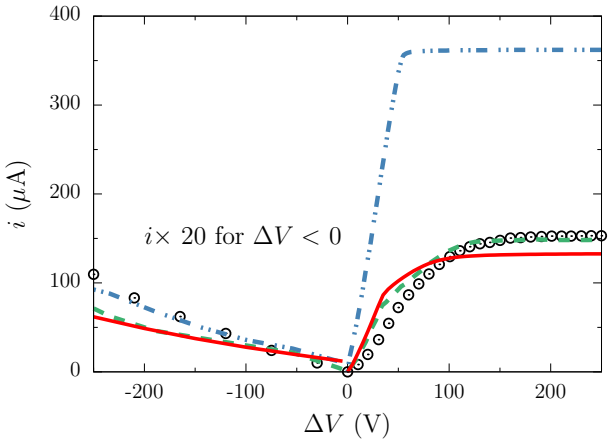

(b) $\Phi = 1.0$

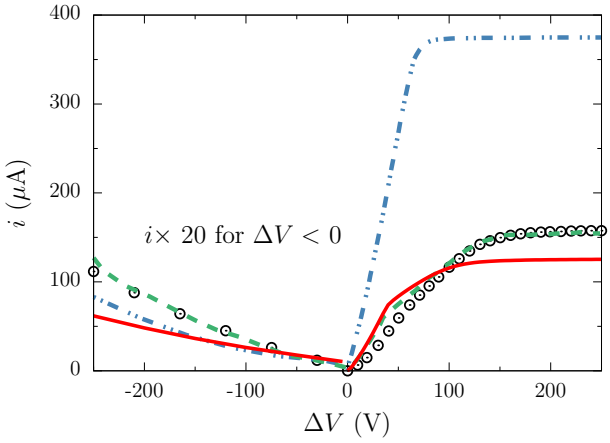

(c) $\Phi = 1.2$

Figure 2. Simulated $i-V$ curves (red lines) in the *HFB flame* with three equivalence ratios compared to experimental data (symbols) and simulation results (blue lines) of Speelman et al. [4]. Results from the optimized model of Speelman et al. [4] are also shown (green lines).

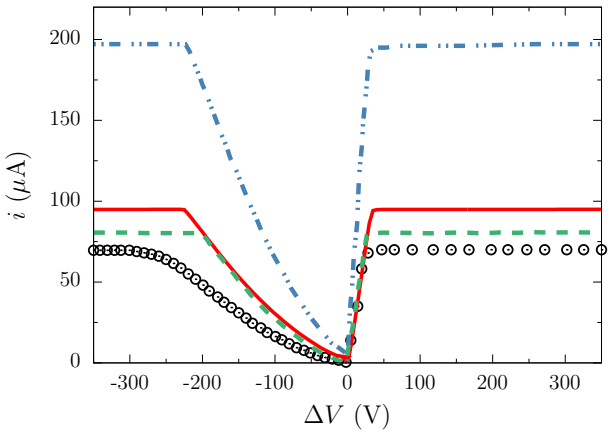

(a) $L = 3.7$ mm

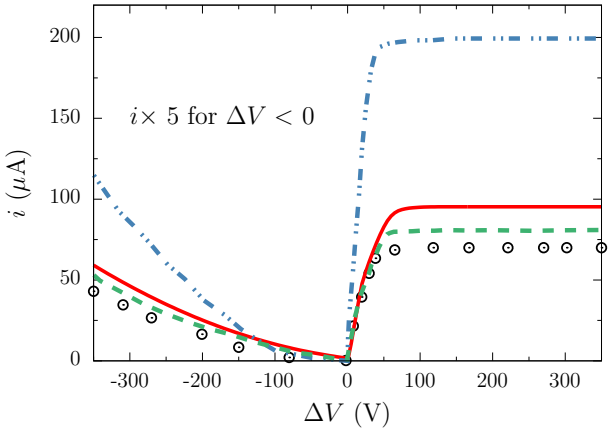

(b) $L = 10$ mm

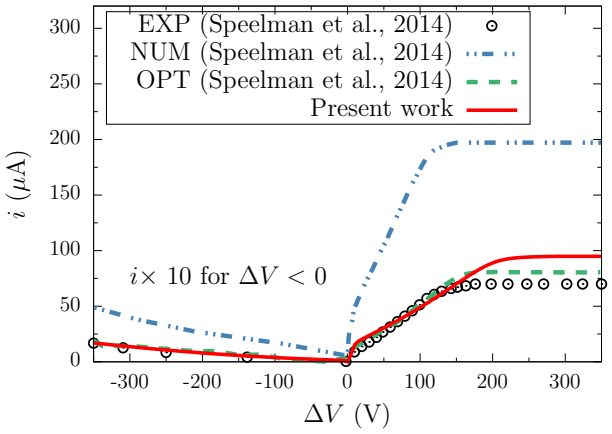

(c) $L = 20$ mm

Figure 3. Simulated $i-V$ curves (red lines) in the *McK flame* for three inter-electrode distances compared to experimental data (symbols) and simulation results (blue lines) of Speelman et al. [3]. Results from the optimized model of Speelman et al. [4] are also shown (green lines).

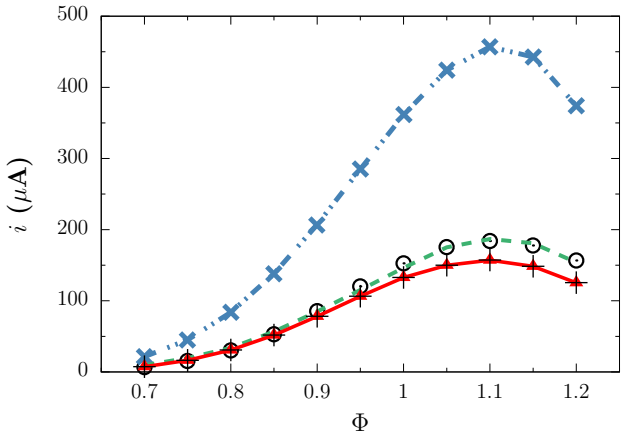

(a) *HFB flame*

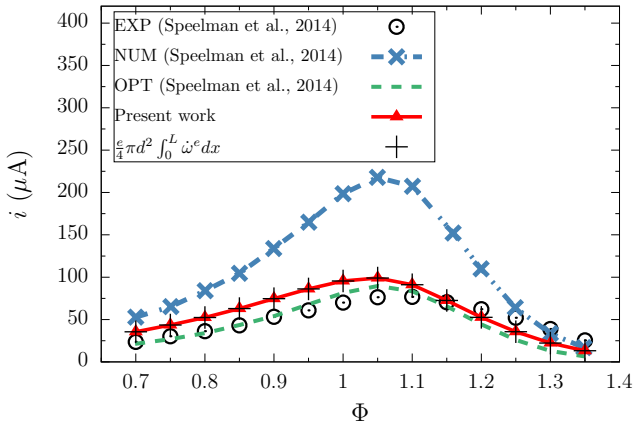

(b) *McK flame*

Figure 4. Evolution of saturation current with equivalence ratio compared to simulations and experiments of Speelman et al. [3,4]. Experimental results are from atmospheric methane/air flames stabilized (a) : on a heat flux burner with $T_u = 350$ K and (b) on a McKenna burner with $T_u = 288$ K. Saturation currents computed from Eq. 18 are also shown.

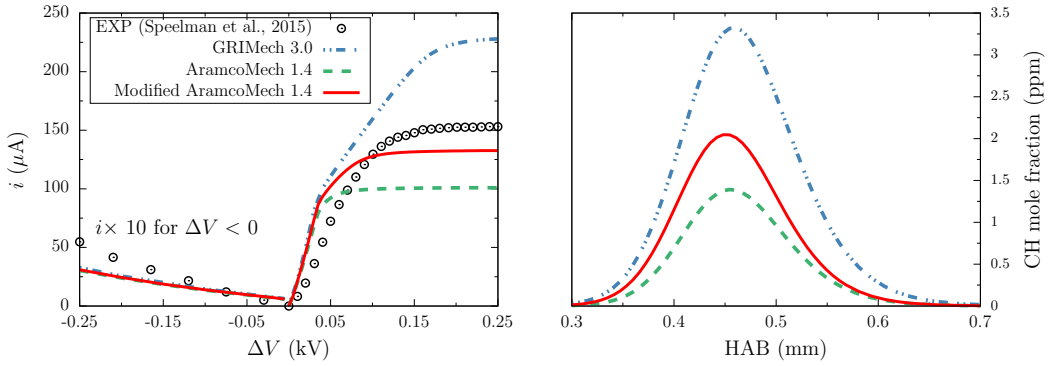

(a) Current versus the applied voltage

(b) CH distribution (all voltages)

Figure 5. Simulated $i-V$ curves and distribution of CH in the *HFB flame* obtained with three neutral reaction mechanisms. Flame parameters are $\Phi = 1$, $p = 1$ atm, $T_u = 350$ K and $\dot{m} = 0.036$ g·cm^{-2}·s^{-1}. In (a), current data for $\Delta V < 0$ are multiplied by 10 for clarity.

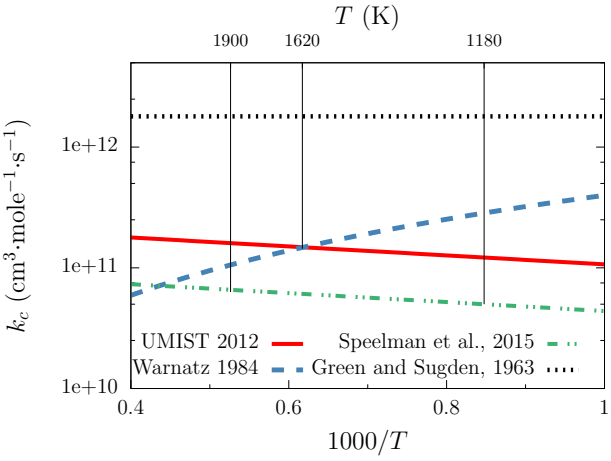

Figure 6. Arrhenius plot of chemi-ionization rate constant.

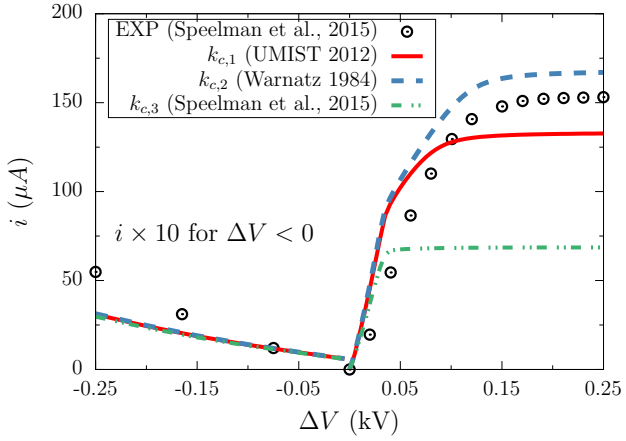

Figure 7. $i-V$ curves in the *HFB flame* at $\Phi = 1$ obtained with various chemi-ionization rates.

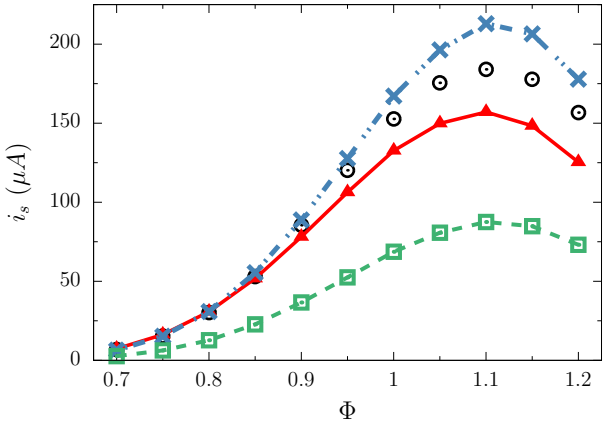

(a) *HBF flame*

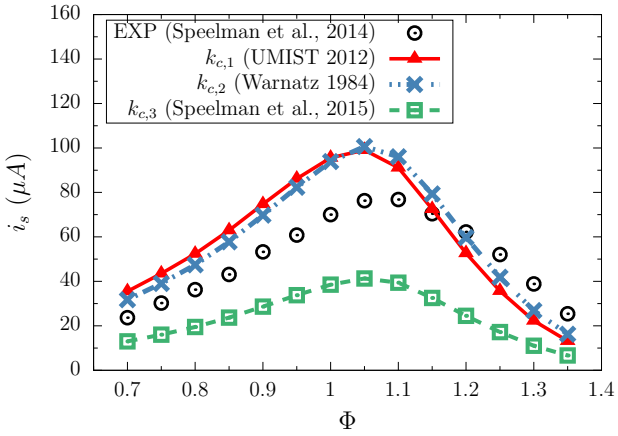

(b) *McK flame*

Figure 8. Saturation currents for various equivalence ratios obtained with different chemi-ionization rates compared to the experiments of Speelman et al. [3,4]. The results are from atmospheric CH_4/air flames stabilized : (a) on a McKenna burner with $T_u = 288$ K and (b) on a heat flux burner with $T_u = 350$ K.

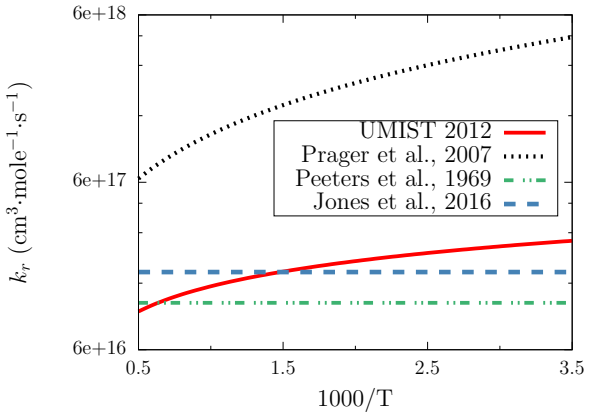

Figure 9. Arrhenius plot of overall recombination rate constant.

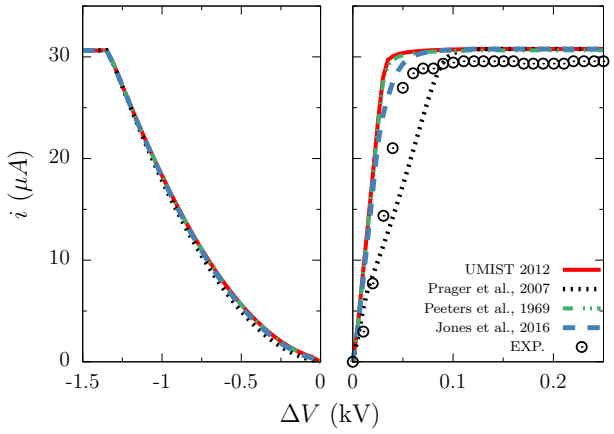

(a) $\Phi = 0.8$

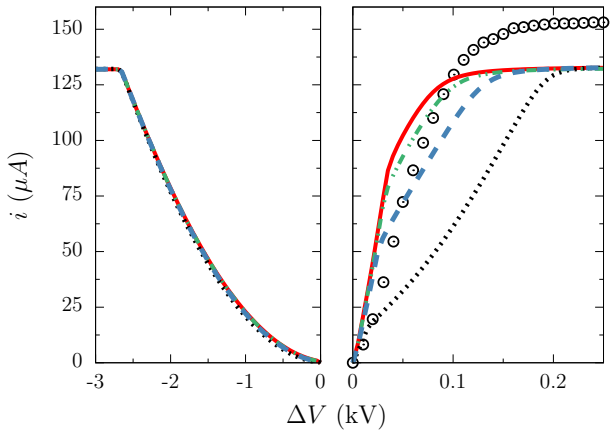

(b) $\Phi = 1.0$

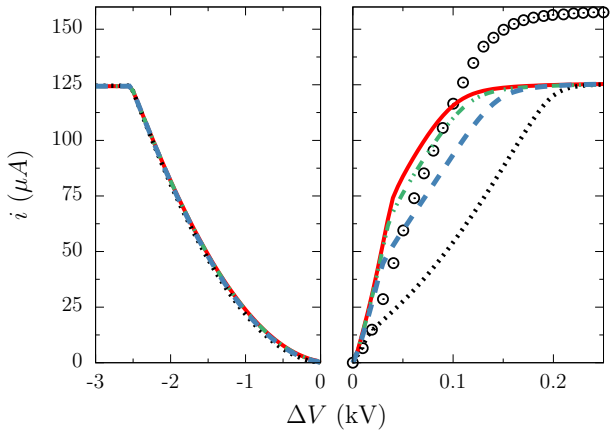

(c) $\Phi = 1.2$

Figure 10. $i-V$ curves in the *HFB flame* obtained with various recombination rates. Modified AramcoMech 1.4 mechanism and $k_{c,1}$ are used in the simulations.

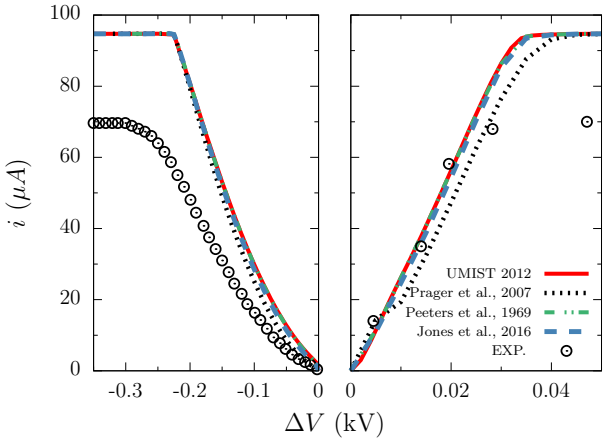

(a) $L = 3.7$ mm

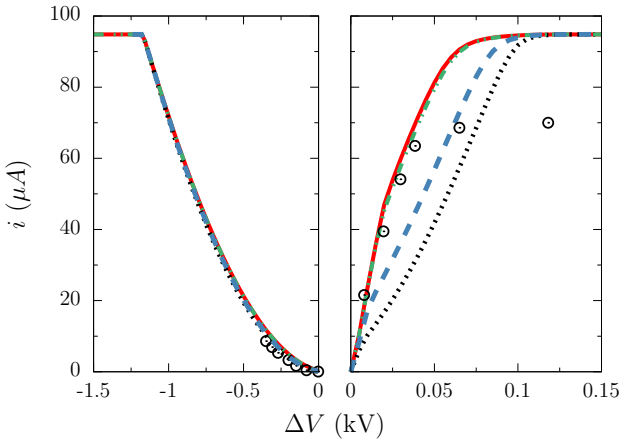

(b) $L = 10$ mm

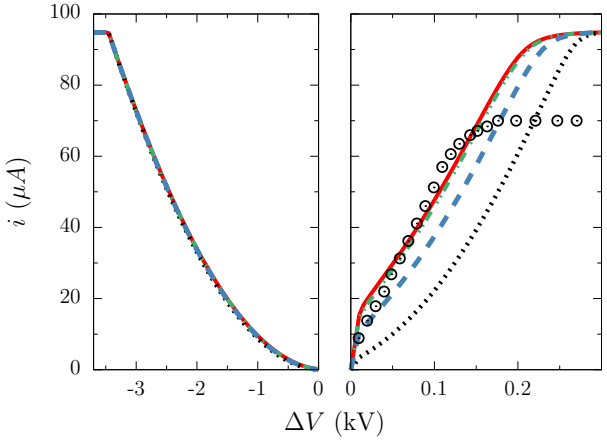

(c) $L = 20$ mm

Figure 11. $i-V$ curves in the *Mck flame* obtained with various recombination rates. Modified AramcoMech 1.4 mechanism and $k_{c,1}$ are used in the simulations.

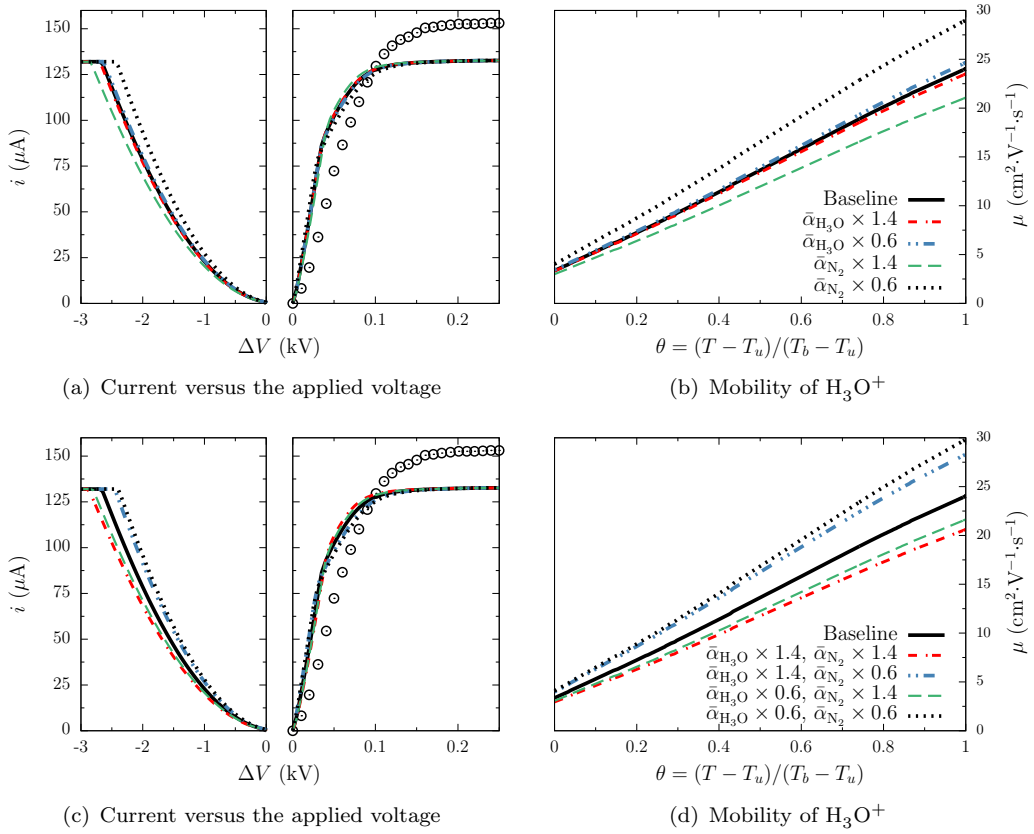

(a) Current versus the applied voltage (b) Mobility of H_3O^+

(c) Current versus the applied voltage (d) Mobility of H_3O^+

Figure 12. $i-V$ curve and mobility of H_3O^+ ion in the $HFBflame$ at $\Phi = 1$ with varying $\bar{\alpha}_{H_3O^+}$ and $\bar{\alpha}_{N_2}$ by $\pm$ 40 % one at a time or simultaneously. Modified AramcoMech 1.4 mechanism, $k_{c,1}$ and $k_{r,UMIST}$ are used in the simulations.

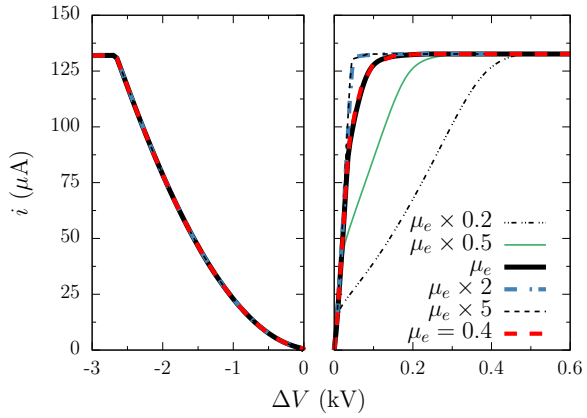

Figure 13. $i-V$ curves in the $HFBflame$ at $\Phi = 1$ by varying electron mobility. Modified AramcoMech 1.4 mechanism, $k_{c,1}$ and $k_{r,UMIST}$ are used in simulations.

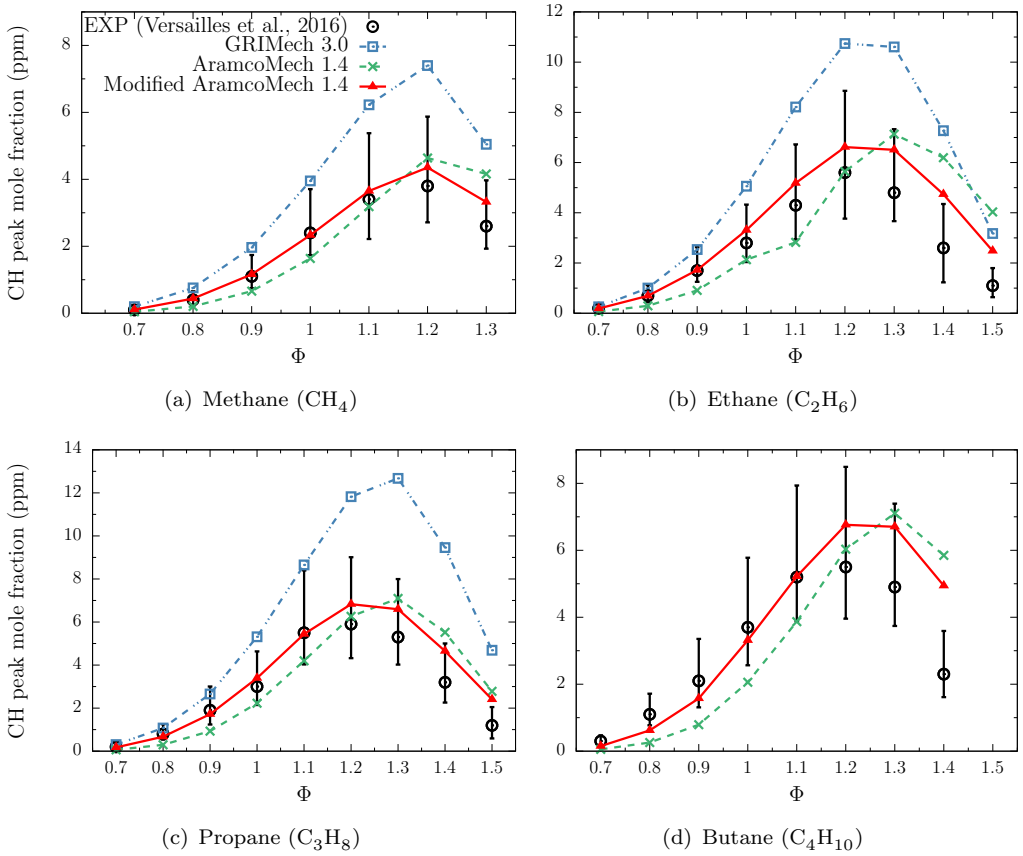

(a) Methane (CH_4)

(b) Ethane (C_2H_6)

(c) Propane (C_3H_8)

(d) Butane (C_4H_{10})

Figure B.1. Peak CH mole fractions for various equivalence ratios with different reaction mechanisms, compared to the experiment of Versailles et al. [21]. CH data is obtained from premixed, laminar, jet-wall stagnation flames burning a mixture of air with methane, ethane, propane, or n-butane. Error-bars are plotted using uncertainty information in Ref. [21].

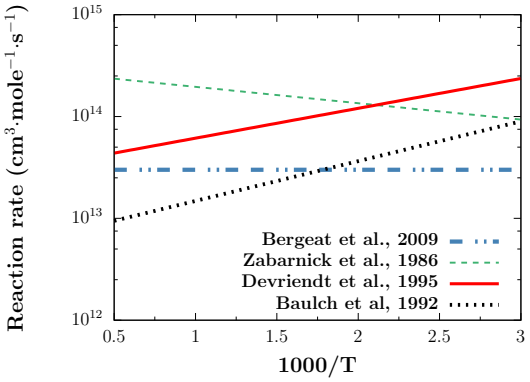

(a) B.R1: $CH_2 + H \rightleftharpoons CH + H_2$

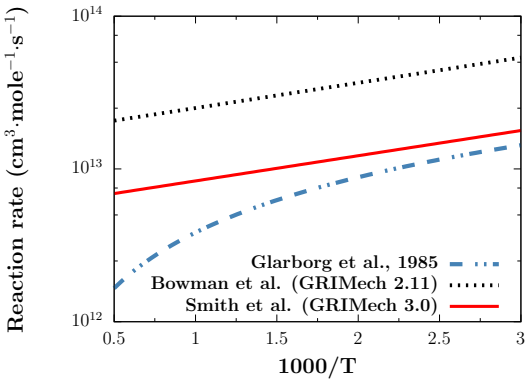

(b) B.R2: $CH + H_2O \rightleftharpoons H + CH_2O$

Figure B.2. Arrhenius plot of reaction rate constant for reactions: (a) $CH_2 + H \rightleftharpoons CH + H_2$ and (b) $CH + H_2O \rightleftharpoons H + CH_2O$. Labels 'Bergeat et al., 2009', 'Zabarnick et al., 1986', 'Devriendt et al., 1995', 'Baulch et al., 1992', 'Glarborh 1985 ', 'Bowman et al.' and 'Smith et al.' refer to reaction rates in Refs. [89], [87], [91], [92], [90], [88] and [60], respectively.

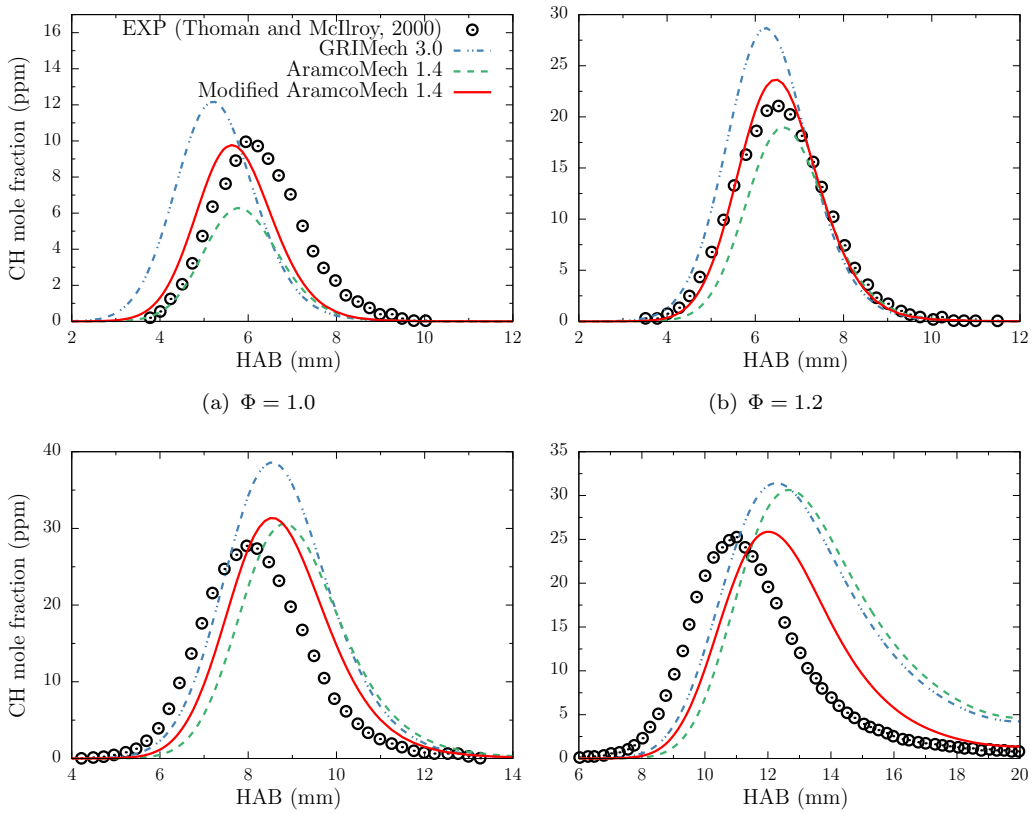

(a) $\Phi = 1.0$ (b) $\Phi = 1.2$

(c) $\Phi = 1.4$ (d) $\Phi = 1.6$

Figure B.3. CH mole fraction as a function of height above the burner for various equivalence ratios, obtained with different reaction mechanisms, compared to the experiment of Thoman et al. [22]. The CH profiles are obtained from 31 Torr, premixed, laminar, burner-stabilized $CH_4/O_2/Ar$ flames.

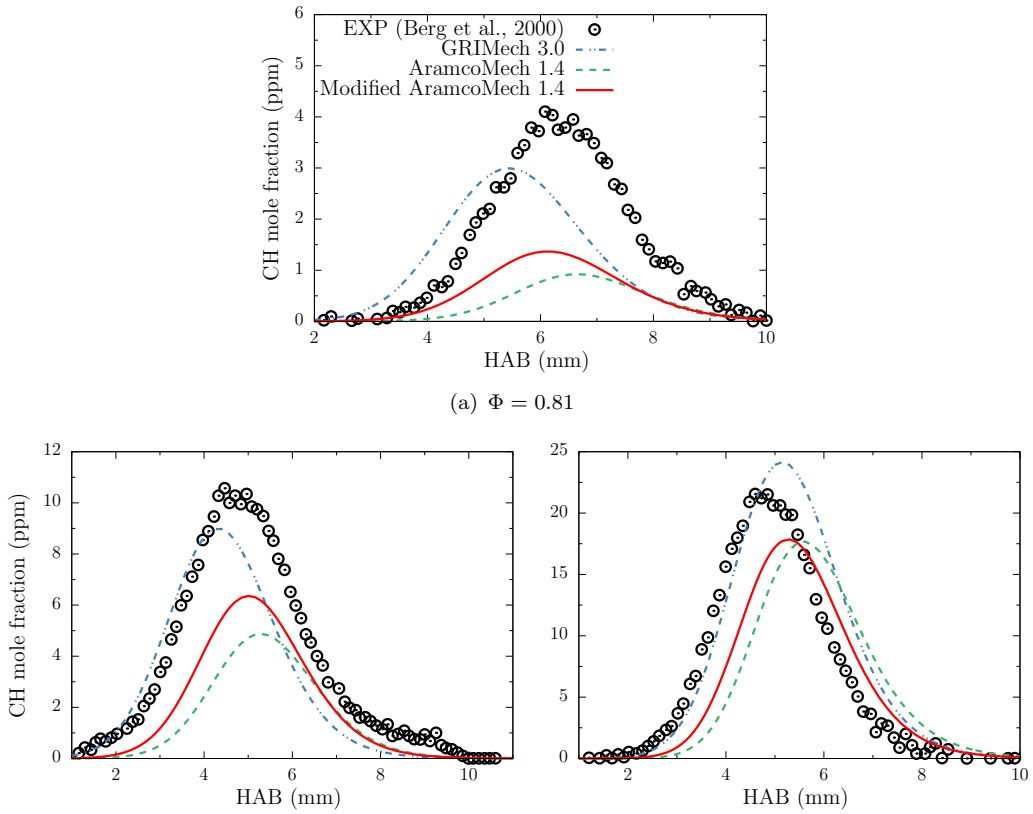

(a) $\Phi = 0.81$

(b) $\Phi = 1.07$

(c) $\Phi = 1.28$

Figure B.4. CH mole fraction as a function of height above the burner for various equivalence ratios, obtained with different reaction mechanisms, compared to the experiment of Berg et al. [23]. The results are obtained from low pressure (30-40 Torr), premixed, laminar, burner-stabilized $CH_4/O_2/N_2$ flames.